

## Chapter 6

# Dynamics and trapping of atoms near dielectric surfaces

### 6.1 Introduction

In this section we investigate the center-of-mass dynamics as well as quantum electrodynamics of single atoms located in close proximity to dielectric surfaces, including in the presence of gravitational, optical dipole, and Casimir-Polder potentials, as well as the stochastic nature of the atom cloud distribution, photon statistics, and atom-photon scattering processes. Interesting insights can be gained from these Monte-Carlo simulations, implemented for the specific system of a silica microtoroidal resonator and cesium atoms, revealing behaviors that are validated by experiments discussed in Chapter 5. Moreover, these provide useful tools in designing optical traps for neutral atoms in close proximity to dielectric boundaries as well as loading schemes, with the specific example of using real-time detection to load atoms into an orbiting optical dipole trap being discussed. This chapter also discusses schemes of trapping neutral atoms near a dielectric surfaces, with specific examples given for a microtoroidal cavity based system, such as an optical tweezer trap, orbiting evanescent far off resonant trap (eFORT), or toroid-nanofiber trap.

In Sec. 6.2, we discuss the dynamics of a specific system of falling cesium atom cloud near a silica microtoroidal resonator, which has been experimentally realized, as discussed in Chapter 5. While in the context of this specific system, many aspects of this simulation are extendable to the general case of single neutral atoms near dielectric surfaces. This includes the effects of dielectric surfaces on the internal states of the atom, such as modifications of atomic spontaneous decay rate and surface-induced shifting atom's electronic energy levels due to the Casimir-Polder effect. In Sec. 6.3, we discuss various atom trapping schemes.

## 6.2 Simulations of atomic trajectories near a dielectric surface

This section is largely based on ref. [228]. Reference [228] refers to the then current literature in 2011 at the time of publication. The work described in this section (Sec. 6.2) is a result of a team collaboration of three authors of the manuscript, whose contributions I would like to acknowledge here. Nate Stern made major contributions in the theoretical formulations discussed in this section, especially in the calculation of atom-surface effects such as the Casimir-Polder potential, and played a major role in the writing of the manuscript. My major contributions are in the design, creation and programming of the simulations performed in this manuscript, development of ideas and theories in this manuscript, and help in the preparation of the manuscript. I would also like to acknowledge Prof. Takao Aoki for his contributions to our microtoroidal cavity QED experimental system, the platform that forms the basis of the context of this manuscript. This work was carried out under the guidance and supervision of my advisor, Prof. Jeff Kimble at Caltech.

In this section, we present a semiclassical model of an atom moving in the evanescent field of a microtoroidal resonator. Atoms falling through whispering-gallery modes can achieve strong, coherent coupling with the cavity at nanoscale distances of approximately 100 nanometers from the surface; in this regime, surface-induced Casimir-Polder level shifts become significant for atomic motion and detection. Atomic transit events detected in recent experiments are analyzed with our simulation, which is extended to consider atom trapping in the evanescent field of a microtoroid.

### 6.2.1 Background

Strong, coherent interactions between atoms and light are an attractive resource for storing, manipulating, and retrieving quantum information in a quantum network with atoms serving as nodes for quantum processing and storage and with photons acting as a long-distance carrier for communication of quantum information [132]. One realization of a quantum node is an optical cavity, where light-matter interactions are enhanced by confining optical fields to small mode volumes. In the canonical implementation, a Fabry-Perot resonator with intracavity trapped atoms enables a panoply of cavity quantum electrodynamics (cQED) phenomena using single photons and single atoms, and thereby, validates many aspects of a cQED quantum node [167, 254].

Despite these achievements, high-quality Fabry-Perot mirror cavities typically require significant care to construct, and complex experimental instrumentation to stabilize. These practical issues

have begun to be addressed by atom chips [193, 81], in which atoms are manipulated in integrated on-chip microcavity structures offering a scalable interface between light and matter [240, 50, 86]. Owing to their high quality factors, low mode volumes, and efficient coupling to tapered optical fibers [11], microtoroidal resonators are a promising example of microcavities well-suited for on-chip cQED with single atoms and single photons [224]. Strong coupling [9, 5] and non-classical regulation of optical fields [57, 10] have been demonstrated with atoms and the whispering-gallery modes of a silica microtoroidal resonator.

In our experiments with microtoroids, Cs atoms are released from an optical trap and fall near a silica toroid, undergoing coherent interactions with cavity modes as each atom individually transits through the evanescent field of the resonator. In the most recent work of [5], atom transits are triggered in real-time to enable measurement of the Rabi-split spectrum of a strongly-coupled cQED system. Whereas a single atom is sufficient to modify the cavity dynamics, falling atoms are coupled to the cavity for only a few microseconds. Atom dropping experiments necessarily involve a large ensemble of individual atomic trajectories and represent, consequently, a far more complex measurement result.

Interactions between a neutral atom and a dielectric surface modify the radiative environment of the atom resulting in an enhanced decay rate [156] and Casimir-Polder (CP) forces [231, 32]. These *perturbative* radiative surface interactions are usually insignificant in cQED experiments with Fabry-Perot resonators where atoms are far from mirror surfaces, but in microcavity cQED, atoms are localized in evanescent fields with scale lengths  $\lambda/2\pi \sim 150$  nm near a dielectric surface. The experimental conditions for microtoroidal cQED with falling atoms in [5] necessarily involve significant CP forces and level shifts while simultaneously addressing strong coupling to optical cavity modes. Theoretical analysis of this experiment requires addressing both the strong atom-cavity interactions and atom interactions with the dielectric surface of the microtoroid. As reported in [5] and discussed in Chapter 5, spectral and temporal measurements offer signatures of both strong coupling to the cavity mode and the significant influence of surface interactions on atomic motion. The role of these effects is quantified with detailed simulation of the trajectories of falling atoms detected in the real-time at low photon numbers.

In this section, we discuss in detail the approach used to simulate atomic motion near the surface of an axisymmetric dielectric resonator under the influence of strong coherent interactions with cavity modes. The experimental detection method of [5] is implemented stochastically in a semiclassical simulation of atom trajectories. These simulations provide a perspective on the atomic motion of

atom transits recorded in our microtoroid experiments, while offering additional insights into the loading of optical evanescent field traps. In section 6.2.2, we outline the semiclassical model of a two-level atom coupled to the whispering gallery modes of a microtoroidal resonator. In section 6.2.3, we review the optical dipole forces which are a critical factor influencing atomic motion in an optical cavity. Our calculations of modified emission rates and Casimir-Polder surface interactions are detailed in section 6.2.4. Section 6.2.5 describes the implementation of our model for simulating recent atom-toroid experiments. Finally, section 6.3.2.1 extends our simulation to evanescent field traps around a microtoroid.

## 6.2.2 Atoms in a microtoroidal cavity

We approach the motion of atoms moving under the influence of surface interactions and coherent cavity dynamics with a semiclassical method to efficiently simulate a large number of atom trajectories. For surface interactions, dispersion forces are calculated *perturbatively* using the linear response functions of SiO<sub>2</sub> and a multi-level atom. For nearly-resonant *non-perturbative* coherent interactions between atom and cavity, the atomic internal state and the cavity field are treated quantum mechanically within the two-level and rotating-wave approximations.

Simulations of atomic motion follow the semiclassical method detailed in [66]. Mechanical effects of light are incorporated classically as a force  $\vec{F}(\vec{r})$  on a point particle atom at location  $\vec{r}$ . Trajectories  $\vec{r}(t)$  are calculated with a Langevin equation approach to incorporate momentum diffusion from fluctuations. At each simulation time step  $t^i$ , the atomic velocity is calculated as:

$$v_j^{i+1} = v_j^i + F_j^i \Delta t / m_{\text{Cs}} + \sqrt{2D_{jj}^i \Delta t / m_{\text{Cs}}^2} W_j^i, \quad (6.1)$$

where  $\vec{v}^i$  is the velocity at the  $i$  time step,  $m_{\text{Cs}}$  is the atomic mass, and  $\Delta t$  is the simulation time step  $t^{i+1} - t^i$ . The  $\vec{W}^i$  are normally distributed with zero mean and standard deviation of one. Given the force  $\vec{F}$  and diffusion tensor  $D_{ij}$  as discussed in section 6.2.3, the atom trajectory  $\vec{r}(t)$  and cavity transmission and reflection coefficients,  $T(t)$  and  $R(t)$ , are calculated. A single atom strongly coupled to the cavity mode has a large effect on cavity fields and optical forces, requiring simultaneous solutions of atomic motion and cQED dynamics.

Full quantization of atomic motion leads to an unwieldy Hilbert space not conducive to efficient simulation. In contrast, semiclassical methods are well-suited for simulating atomic motion in experiments with falling atoms near resonators. The ratio of the recoil energy to the linewidth of the cesium  $6S_{1/2} \rightarrow 6P_{3/2}$  transition is less than  $10^{-3}$ . Further, the recoil velocity of  $\sim 3.5$  mm/s is

much less than the typical velocity of falling atoms of order 200 mm/s so that each spontaneous emission event represents a small momentum kick. Cavity fields and internal atomic states respond quickly to environment changes, allowing calculation of optical forces and momentum diffusion in a constant-velocity limit at time  $t$  and energy shifts from surface interactions as if the atom were stationary. Overall simulation accuracy is limited by uncertainty in input parameters such as field strength, couplings, geometry, and approximations for the force, not by the semiclassical approximation for atomic center-of-mass motion. The remainder of this section discusses the quantum mechanical equations of motion for the atom and cavity fields in the low-probe intensity limit, to be followed later by contributions to the force  $\vec{F}$  used in (6.1).

### 6.2.2.1 Modes of a microtoroidal resonator

Refer to Sec. 3.1.1.1 for discussion of this topic.

### 6.2.2.2 Cavity QED in an axisymmetric resonator

Please refer to Sec. 3.1.1.3 for discussion of this topic.

## 6.2.3 Optical forces on an atom in a cavity

Neutral atoms experience forces from the interaction of the atomic dipole moment with the radiation field. These optical dipole forces have a quantum mechanical interpretation as coherent photon scattering [92, 55]. For a light field near resonance with the atomic dipole transition, these optical forces can be quite strong, even at the single photon level; cavity-enhanced dipole forces [66, 108] have been exploited to trap [107] and localize [187] a single atom with the force generated by a single strongly-coupled photon. In this section, we discuss how the optical forces, their first-order velocity dependence, and their fluctuations are included in our semiclassical simulation.

### 6.2.3.1 Dipole forces

In a quantum mechanical treatment of light-matter interactions [55], the eigenstates of the system are dressed states of atom and optical field. The quantum mechanical optical force on the atom at location  $\vec{r}$  can be found from the commutator of the atom momentum  $\vec{p}$  with the interaction Hamiltonian  $H_{\text{int}}$  consisting of the last two terms from the Hamiltonian (5.1):

$$\vec{F} = \frac{d\vec{p}}{dt} = \frac{i}{\hbar} [H_{\text{int}}, \vec{p}] = -\hbar \nabla g_{\text{tw}}^*(\vec{r}) (a^\dagger \sigma^- + \sigma^+ b) - \hbar \nabla g_{\text{tw}}(\vec{r}) (\sigma^+ a + b^\dagger \sigma^-). \quad (6.2)$$

The gradient from the position space representation of the momentum operator  $\vec{p}$  only acts on  $g_{\text{tw}}(\vec{r})$  and not on the field operators [244, 67]. The steady-state expectation values of (6.2) give the dipole force on the atom in the semiclassical approximation:

$$\begin{aligned} \langle \vec{F} \rangle_{\text{ss}} = & -\hbar \nabla g_{\text{tw}}^*(\vec{r}) (\langle a^\dagger \rangle_{\text{ss}} \langle \sigma^- \rangle_{\text{ss}} + \langle \sigma^+ \rangle_{\text{ss}} \langle b \rangle_{\text{ss}}) \\ & -\hbar \nabla g_{\text{tw}}(\vec{r}) (\langle \sigma^+ \rangle_{\text{ss}} \langle a \rangle_{\text{ss}} + \langle b^\dagger \rangle_{\text{ss}} \langle \sigma^- \rangle_{\text{ss}}). \end{aligned} \quad (6.3)$$

As described in section 6.2.2, the steady-state operator expressions are simplified by reducing expectation values of operator products to products of linearized steady-state operator expectation values. Ignoring fiber and spontaneous emission losses, an effective conservative dipole potential  $U_{\text{d}}$  can be defined by integration of (6.3).

### 6.2.3.2 Velocity-dependent forces on an atom

Non-zero velocity effects on the force (6.3) are found by including a first-order velocity correction in the steady state expectation values [80, 92, 67]. Consider a vector of operators  $\vec{O}$  whose expectation values obey a linearized equation system such as (3.15). Assuming a small velocity, we expand the operator expectation values  $\langle \vec{O} \rangle$  as:

$$\langle \vec{O} \rangle = \langle \vec{O} \rangle_0 + \langle \vec{O} \rangle_1 + \dots, \quad (6.4)$$

where the subscripts denote the order of the velocity  $v$  in each term. If an atom is moving through these fields, then the cavity parameters depend in general on atomic position  $\vec{r}$ . As  $\vec{r}$  changes in time, the fields must evolve in response. Consequently, the time derivative of the expectation value evolves not only from explicit time dependence, but from atomic motion as well.

$$\langle \dot{\vec{O}} \rangle = \left( \frac{\partial}{\partial t} + \vec{v} \cdot \vec{\nabla} \right) \langle \vec{O} \rangle. \quad (6.5)$$

Setting the explicit time derivatives in (6.5) to zero, the perturbative expansion of the time derivative can be equated to the original linearized equation system. Collecting terms of each order in velocity gives an equation for the first-order term  $\langle \vec{O} \rangle_1$  in terms of the zero-velocity steady-state solution  $\langle \vec{O} \rangle_0$ . This procedure requires the spatial derivative of the zero-order steady-state solutions, where spatial dependence enters through the atomic transition frequency  $\omega_{\text{a}}(\vec{r})$ , the spontaneous emission rate  $\gamma(\vec{r})$ , and the atom-cavity coupling  $g(\vec{r})$ . The steady-state solutions  $\langle \vec{O} \rangle$  to first order in velocity

are then used to calculate a velocity-dependent optical force  $\vec{F}(\vec{r})$  in (6.3). Only terms linear in velocity are kept in the operator products in (6.3). However, these friction terms, while included for completeness, do not have a significant influence on calculated spectra or time-dependent trajectories.

In practice, first-order velocity corrections are small in our simulation. For example, Doppler shifts arising from spatial derivatives of the cavity modes are on the order of  $\vec{k} \cdot \vec{v}$ , where  $\vec{k}$  is the mode wavevector. For typical azimuthal velocities of less than 0.1 m/s, the Doppler shift is less than 1 MHz. The effect becomes more significant as atoms accelerate to high velocities near the surface, but atomic level shifts from surface interactions are more significant in this regime than the Doppler shifts. Frictional forces not related to the cavity-enhanced mode, i.e., Casimir-Polder forces on moving atoms, are not included in the simulation since they are extremely weak and short-ranged for ground state atoms [210].

### 6.2.3.3 Momentum diffusion and the diffusion tensor in a cavity

Quantum fluctuations of optical forces are treated by adding a stochastic momentum diffusion contribution to the atomic velocity in the Langevin equations of motion. We calculate the diffusion tensor components used in (6.1),  $D_{ii}$ , using general expressions for diffusion in an atom-cavity system generalized for the two-mode cavity of a toroid [170]:

$$2D_{ii} = (\hbar k)^2 2\gamma |\langle \sigma^- \rangle_{\text{ss}}|^2 + |\hbar \nabla_i \langle \sigma^- \rangle_{\text{ss}}|^2 2\gamma + 2\kappa \left( |\hbar \nabla_i \langle a \rangle_{\text{ss}}|^2 + |\hbar \nabla_i \langle b \rangle_{\text{ss}}|^2 \right), \quad (6.6)$$

for  $i = x, y, z$ , where  $\gamma$  is the atomic field spontaneous decay rate. The first term represents fluctuations from spontaneous emission, the second term describes a fluctuating atomic dipole coupled to a cavity field, and the third represents a fluctuating cavity field coupled to an atomic dipole. (6.6) is approximated using steady-state fields calculated from the linearized solutions to the master equation (3.18). Although included in the trajectory model, momentum diffusion does not significantly alter averages over ensembles of trajectories at the weak excitation levels and low atomic velocities used in the relevant experiments.

### 6.2.4 Effects of surfaces on atoms near dielectrics

In the vicinity of a material surface, the mode structure of the full electromagnetic field is modified due to the dielectric properties of nearby objects. These off-resonant radiative interactions modify the dipole decay rate of atomic states and shift electronic energy levels. This surface interaction varies spatially as the relative atom-surface configuration changes. The surface phenomena are

dispersive and depend on the multi-level description of the atom's electronic structure; they are calculated using traditional perturbation theory with the full electromagnetic field without focusing on a few select modes enhanced by a cavity in cQED.

#### 6.2.4.1 Spontaneous emission rate near a surface

When a classical oscillating dipole is placed near a surface, its radiation pattern is modified by the time-lagged reflected field from the dielectric surface. The spontaneous emission rate oscillates with distance  $d$  from the surface, which can be interpreted as interference between the radiation field of the dipole and its reflection. The variation of the emission rate depends on whether the dipole vector is parallel or perpendicular to the surface, as intuitively expected from the asymmetry of image dipole orientations of dipoles aligned parallel and perpendicular to the surface normal. For either orientation, the spontaneous emission rate features a marked increase within a wavelength of the surface due to surface evanescent modes that become available for decay for  $d \lesssim \lambda_0$ . The decay rate diverges as  $(\lambda/2d)^3 \text{Im}(\epsilon)$  for small  $d$  due to absorption, but this regime is not relevant in the present cQED transmission simulations because fast-moving atoms spend a negligible amount of time at vanishing  $d$  and, further, surface-induced level shifts also scaling as  $d^{-3}$  bring the atom out of resonance near the surface (section 6.2.4.2).

We calculate the surface-modified dipole decay rates  $\gamma_s^{(\parallel)}(d)$  and  $\gamma_s^{(\perp)}(d)$  for a cesium atom near an SiO<sub>2</sub> surface following the methods of Refs. [156, 149] (see Fig. 6.1). This calculation involves an integration of surface reflection coefficients over possible wavevectors of radiated light. The integrand depends on the dielectric function of SiO<sub>2</sub> evaluated at the frequency  $\omega_a$  of the atomic transition. The orientations refer to the alignment of a classical dipole relative to the surface plane.

#### 6.2.4.2 Calculation of Casimir-Polder potentials

Radiative interactions with a surface are important components of motion for neutral atoms within a few hundred nm of a surface, with the potential for manipulating atomic motion through attractive [231] or repulsive forces [169]. Depending on the theoretical framework, these forces are naturally thought of as radiative self-interactions between two polarizable objects, fluctuations of virtual electromagnetic excitations, or as a manifestation of vacuum energy of the electromagnetic field. These surface interactions, represented by a conservative potential  $U_s$ , are sensitive to the frequency dispersion of the electromagnetic response properties of the atoms and surfaces.

For an atom located a short distance  $d \ll \lambda_0$  from a dielectric, the fluctuating dipole of the atom

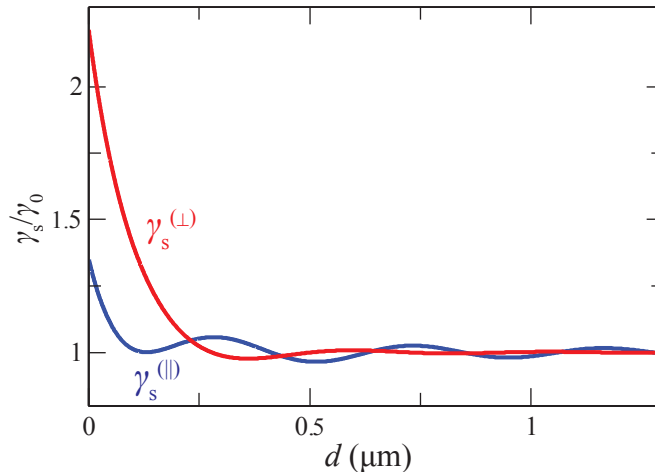


Figure 6.1: **Variations of the dipole decay rate  $\gamma_s(d)$  for a dipole oriented parallel ( $\parallel$ ) and perpendicular ( $\perp$ ) to the surface normal as a function of distance  $d$  from a semi-infinite region of  $\text{SiO}_2$ .** The decay rate is in units of the vacuum decay rate  $\gamma_0$  and the wavelength of the transition is  $\lambda = 852$  nm.

interacts with its own surface image dipole in the well-known nonretarded van der Waals interaction. Using only classical electrodynamics with a fluctuating dipole, the surface interaction potential is found to take the Lennard-Jones (LJ) form  $U_s^{\text{LJ}} = -C_3/d^3$ , where  $C_3$  is a constant that depends on the atomic polarizability and dielectric permittivity of the surface [153, 154, 146, 79]. At larger separations, virtual photons exchanged between atoms and surfaces cannot travel the distance in time  $t \sim 1/\omega$  due to the finite speed of light. Consequently, the interaction potential is reduced, as first calculated in the 1948 paper by Casimir and Polder [38]. The retarded surface potential takes the form  $U_s^{\text{ret}} = -C_4/d^4$  for a constant  $C_4$ , where  $C_4$  depends on both  $c$  and  $\hbar$  as this is fundamentally both a relativistic and quantum phenomenon. The full theory of surface forces for real materials with dispersive dielectric functions came with the work of Lifshitz [150, 72]. This framework reduces to both the above situations for the proper limits, and, importantly, it accounts for finite temperatures, predicting a  $U_s^{\text{th}} \propto d^{-3}$  potential caused by thermal photons dominant at large distances for  $d \gg \hbar c/k_B T$  [7]. In our discussion, we refer to these generalized dispersion forces as *Casimir-Polder* (CP) forces, whereas  $U_s^{\text{LJ}}$ ,  $U_s^{\text{ret}}$ , and  $U_s^{\text{th}}$  refer to the appropriate distance limits.

In microcavity cQED, evanescent field distance scales are set by the scale length of the evanescent field,  $\lambda_0 = \lambda_0/2\pi = 136$  nm (for the Cs  $D_2$  line). The relevant distances ( $0 < d \lesssim 300$  nm) span both the LJ and retarded regimes, but are much shorter than the thermal regime ( $d > 5 \mu\text{m}$ ). In the transition region, the limiting power laws do not fully describe  $U_s$  over the relevant range of  $d$ . In our modeling, we utilize a calculation of  $U_s$  with the Lifshitz approach. The Lennard-Jones,

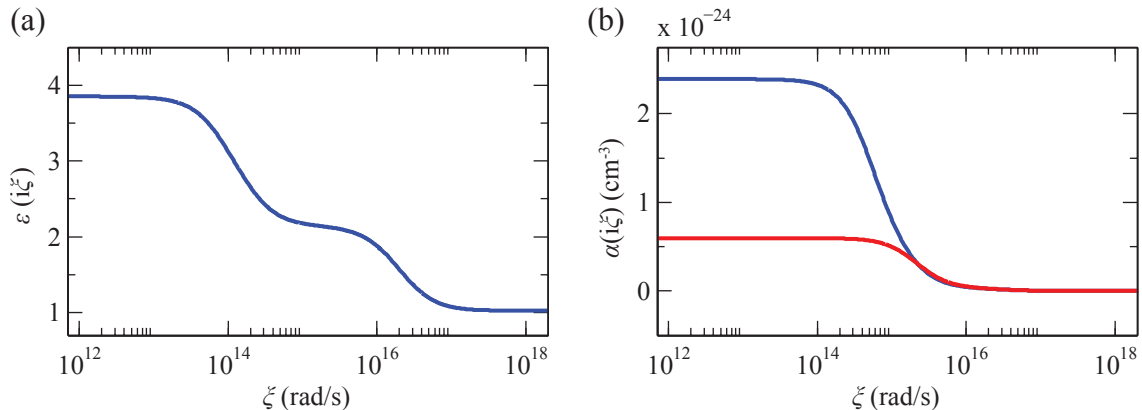


Figure 6.2: **Dispersive response functions for SiO<sub>2</sub> and cesium atoms.** (a) The dielectric function  $\epsilon(i\xi)$  for SiO<sub>2</sub> evaluated for frequency  $\xi$  along the imaginary axis. (b) Total atomic polarizability  $\alpha(i\xi)$  evaluated for frequency  $\xi$  along the imaginary axis for the  $6S_{1/2}$  ground state (red) and the  $6P_{3/2}$  excited state (blue) of cesium calculated as described in 6.2.6.

retarded, and thermal limits arise naturally from the Lifshitz formalism [7].

The potential  $U_s$  enters our simulation in two ways. First, the transition frequency  $\omega_a$  of the two-level atomic system shifts away from the vacuum frequency by  $\delta_a = (U_s^{\text{ex}}(\vec{r}) - U_s^{\text{g}}(\vec{r}))/\hbar$ , where  $U_s^{\text{g}}(\vec{r})$  and  $U_s^{\text{ex}}(\vec{r})$  are the surface potentials for the ground and excited states, respectively. Since the atom transitions between the ground and excited states during its passage through the mode, the average net force used in calculations is found by weighting each contribution by the steady-state atomic state populations,  $F_s = F_s^{\text{g}}(1 - \langle\sigma^\dagger\rangle_{\text{ss}}\langle\sigma\rangle_{\text{ss}}) + F_s^{\text{ex}}\langle\sigma^\dagger\rangle_{\text{ss}}\langle\sigma\rangle_{\text{ss}}$ .

We calculate  $U_s^{\text{g}}$  and  $U_s^{\text{ex}}$  for a cesium atom near a glass SiO<sub>2</sub> surface using the Lifshitz approach. This calculation depends on the dispersion properties of the response functions of materials, in this case the polarizability of the Cs ground state  $\alpha(\omega)$  and the complex dielectric function  $\epsilon(\omega)$  of the silica surface. Modeling of these functions is discussed in 6.2.6. In particular, these response functions must be evaluated on the imaginary frequency axis  $\omega = i\xi$ , as shown in Figure 6.2.

Following the proximity force approximation of [29], curvature of the toroid surface is implemented by treating the toroid as a cylinder with radius of curvature  $R = D_m/2$ . The major axis curvature is neglected because for all relevant distances  $d \ll D_M/2$ . The resulting formula can be interpreted as a sum over discrete Matsubara frequencies  $\xi_n = 2\pi n k_B T/\hbar$  with an integration over transverse wave vectors, which we quote without derivation [29]:

$$U_{\text{surf}}(d) = -k_B T \sqrt{\frac{R}{R+d}} \sum_{n=0}^{\infty} \alpha(i\xi_n) \int_0^{\infty} k_{\perp} dk_{\perp} e^{-2q_n d} \left[ q_n - \frac{1}{4(R+d)} \right] \left\{ 2r_{\parallel}(i\xi_n, k_{\perp}) + \frac{\xi_n^2}{q_n^2 c^2} [r_{\perp}(i\xi_n, k_{\perp}) - r_{\parallel}(i\xi_n, k_{\perp})] \right\}. \quad (6.7)$$

Here,  $\alpha(i\xi_n)$  is the atomic polarizability and  $r_{\parallel,\perp}(i\xi_n, k_{\perp})$  are the reflection coefficients of the dielectric material evaluated for imaginary frequency  $i\xi_n$ . The primed summation implies a factor of  $1/2$  for the  $n = 0$  term. The reflection coefficients for the two orthogonal light polarizations are:

$$r_{\parallel}(i\xi_n, k_{\perp}) = \frac{\epsilon(i\xi_n)q_n - k_n}{\epsilon(i\xi_n)q_n + k_n}, \quad (6.8)$$

$$r_{\perp}(i\xi_n, k_{\perp}) = \frac{k_n - q_n}{k_n + q_n}, \quad (6.9)$$

where

$$q_n = \sqrt{k_{\perp}^2 + \frac{\xi_n^2}{c^2}}, \quad k_n = \sqrt{k_{\perp}^2 + \epsilon \frac{\xi_n^2}{c^2}}, \quad (6.10)$$

and  $\epsilon(i\xi_n)$  is the complex dielectric function evaluated for imaginary frequencies  $i\xi_n$ . Depending on the author,  $r_{\parallel}$  ( $r_{\perp}$ ) is sometimes referred to as  $r_{\text{TM}}$  ( $r_{\text{TE}}$ ).

$U_s^g$  is calculated by numerical evaluation of (6.7).  $U_s^{\text{ex}}$  is also calculated using (6.7), but with an additional contribution accounting for real photon exchange from the excited state with the surface, which is proportional to  $\text{Re} \left[ \frac{\epsilon(\omega_a) - 1}{\epsilon(\omega_a) + 1} \right]$  in the LJ limit [79, 93].

The atom-surface potential  $U_s^g$  for the ground state of cesium near a  $\text{SiO}_2$  surface is shown in Fig. 6.3, including calculations for both a planar and a cylindrical surface. Without the cylindrical correction, the potential approaches the LJ, retarded, and thermal limits at appropriate distance scales. For the planar dielectric, our calculation yields  $C_3/h = 1178 \text{ Hz } \mu\text{m}^3$  and  $C_4/h = 158 \text{ Hz } \mu\text{m}^4$  for the LJ and retarded limits. Note that the transition region between LJ and retarded regimes occurs around  $d \sim 100 \text{ nm}$ , the relevant distance scale for the experiments we are modeling. The effect of the proximity force approximation for the cylindrical cross-section is less than our calculational precision in the region close to the toroid surface ( $d \lesssim 300 \text{ nm}$ ). For  $d > D_m$ , the proximity force approximation method accounting for the curvature is no longer accurate [29], but at these distances, the surface forces are insignificant to atomic motion due to their steep power law fall-off. The excited state potential  $U_s^{\text{ex}}$  has a similar form to  $U_s^g$  (see the blue curve in Fig.6.3), with the C3 coefficient for the excited state given by  $C_3^{\text{ex}}/h \simeq 2C_3^g/h = 2356 \text{ Hz } \mu\text{m}^3$ , where  $C_3^g/h = 1178 \text{ Hz } \mu\text{m}^3$  is the ground state C3 coefficient.

### 6.2.5 Simulating atoms detected in real-time near microtoroids

In order for the semiclassical model to be applied to our falling atom experiments, we must simulate the atom detection processes. In particular, in [5], falling Cs atoms are detected with real-time photon counting using a field programmable gate array (FPGA), with subsequent probe modulation

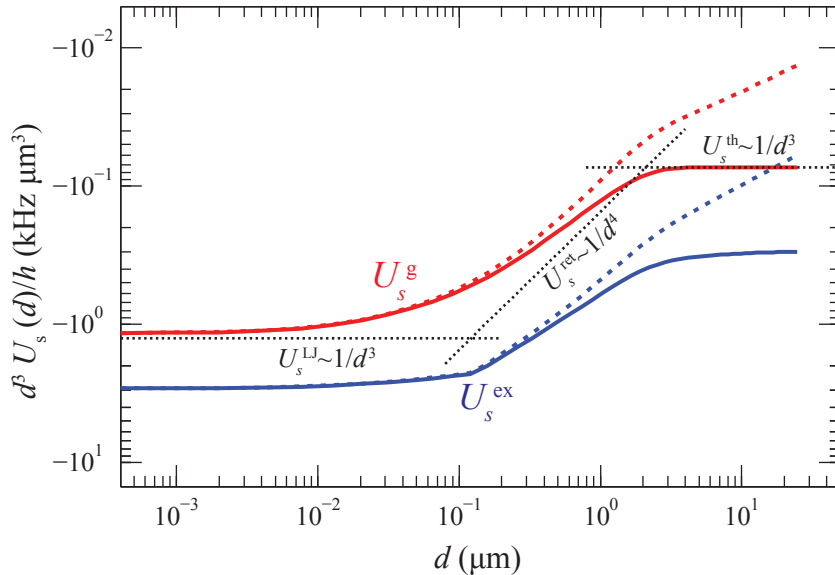


Figure 6.3: **Atom-surface potentials  $U_s^g$  (red) and  $U_s^{ex}$  (blue) for a cesium atom at distance  $d$  from an  $\text{SiO}_2$  surface.** The solid lines are for a planar surface whereas the dashed lines are for a curved surface with radius of curvature  $R = D_m/2 = 1.5 \mu\text{m}$ . The limiting regimes for  $U_s^g$  with a planar surface are shown as dotted lines, each calculated from analytic expressions not using the Lifshitz formalism. The cylindrical surface correction weakens the potential, which is noticeable in the retarded and thermal regimes.

triggered by atom detection.

A microtoroidal cavity with frequency  $\omega_c$  is locked near the  $6S_{1/2}, F = 4 \rightarrow 6P_{3/2}, F = 5$  atomic transition of Cs at  $\omega_a^0$  at desired detuning  $\Delta_{ca} = \omega_c - \omega_a^{(0)}$ . Fiber-cavity coupling is tuned to critical coupling where the bare cavity transmission vanishes,  $T \lesssim T_{\min} \simeq 0.01$ . For atom detection, a probe field at frequency  $\omega_p = \omega_c$  and flux  $P_{\text{in}} \sim 15 \text{ cts}/\mu\text{s}$  is launched in the fiber taper and the transmitted output power  $P_T$  is monitored by a series of single photon detectors. Photoelectric events in a running time window of length  $\Delta t_{\text{th}}$  are counted and compared to a threshold count  $C_{\text{th}}$ . A single atom disturbs the critical coupling balance so that  $T/T_{\min} > 1$ , resulting in a burst of photons which correspond to a possible trigger event. Details of the experimental procedure are given in Chapter 5.

Whereas only a single atom is required to produce a trigger, spectral and temporal data are accumulated over many thousands of trigger events since each individual atom is only coupled to the cavity for a few microseconds. Simulation is a valuable technique to disentangle atomic dynamics from the aggregate data and offer insights into the atomic motion which underlies the experimental measurements.

### 6.2.5.1 Simulation procedure

Central to our simulations is the generation of a set of  $N$  representative atomic trajectories for the experimental conditions of atoms falling past a microtoroid fulfilling the criteria for real-time detection. Since experimental triggering is stochastic, the trajectory set is generated randomly as well. For each desired collection of experimental parameters  $\mathcal{P}$ , a set of semiclassical atomic trajectories  $\{\vec{r}_j(t)\}_{\mathcal{P}}$  is generated that satisfies the detection trigger criteria. This ensemble is used to extract the cavity output functions  $T(t, \Delta_{\text{ap}})$  and  $R(t, \Delta_{\text{ap}})$ . For each individual trajectory,  $t = 0$  is defined to be the time when the trajectory is experimentally triggered by the FPGA. For each set  $\mathcal{P}$ ,  $N$  is chosen large enough for a sufficient ensemble average to be obtained for the final output functions, typically at least 400 unique triggered trajectories.

Within each simulation, the probe field is fixed to a given  $\omega_p$ . Cavity behavior is determined by the parameters  $\omega_c$ ,  $h$ ,  $\kappa_i$ , and  $\kappa_{\text{ex}}$ .  $h$  and  $\kappa_i$  are determined from measurements of the bare cavity with no atoms present. Low-bandwidth fluctuations in  $\kappa_{\text{ex}}$  and  $\omega_c$  from mechanical vibration and temperature locking are modeled as normally distributed random variations with standard deviations of 3 MHz and 1.5 MHz, respectively, that are fixed once for the duration of each simulated trajectory. Similar to the experimental procedure, we impose that the bare-cavity output flux is less than 0.4 cts/ $\mu\text{s}$  at critical coupling and on resonance. This rate would be identically zero for  $\Delta_{\text{cp}} = 0$  and critical coupling in the absence of these fluctuations. If the noise threshold is not met, then the particular trajectory is thrown out as it would have been in experiments.

The atomic cloud is characterized by its temperature, size, and its height above the microtoroid. Its shape is assumed to be Gaussian in each direction with parameters determined by fluorescence imaging. For each simulation loop, an initial atomic position  $\vec{r}_{\text{in}}$  is selected from the cloud and the initial velocity  $\vec{v}_{\text{in}}$  is selected from a Maxwell-Boltzmann distribution of temperature  $T$ . The trajectory is propagated forward in time under the influence of gravity until it crosses the toroid equatorial plane at  $z = 0$ . Only trajectories which pass within 1  $\mu\text{m}$  of the toroid surface at  $z = 0$  are kept as a candidate for detection, as atoms outside of this annulus have negligible probability of triggering due to their weak coupling to the optical mode. Once an acceptable set of initial conditions is obtained, the trajectory  $\vec{r}(t)$  is calculated over a 50  $\mu\text{s}$  time window starting 20  $\mu\text{s}$  before its crossing of  $z = 0$ , this time with the gravity, optical dipole forces, and surface interactions included. As the atom moves through the cavity mode, the atom-cavity coupling  $g$ , level shifts, decay rates, and forces change with position  $\vec{r}$ , causing deviations of the trajectory from the preliminary free-fall trajectory. If the atom crashes into the surface of the toroid, then the coupling is set to

$g = 0$  from then onwards and the trajectory effectively ends (except for random ‘noise’ photon counts arising from the non-zero background transmission).

Using  $\vec{r}(t)$  and the steady-state expressions for the fields (section 6.2.2), we find the transmission  $T(t)$ . The photon count record  $C_i(t_j)$  on each photodetector  $i$  for time step  $t_j$  is generated from a time-dependent Poisson process with mean count per bin of  $\overline{C}_i(t_j) = T(t_j)P_{\text{in}}\Delta t$ , where  $\Delta t = t_{j+1} - t_j = 1$  ns and  $P_{\text{in}}$  is the input flux. Since the typical flux is  $P_{\text{in}} \sim 10$  MHz and the time scale of quantum correlations is  $\sim 10$  ns, the photon count process is assumed to be Poissonian on the relevant timescale of a few hundred nanoseconds for atom detection. The count record  $C_i(t_j)$  is compared to the desired threshold of  $C_{\text{th}}$  in a time window  $\Delta t_{\text{th}}$  [5]. If the trigger condition is met, the initial conditions  $\vec{r}_{\text{in},j}$ ,  $\vec{v}_{\text{in},j}$ , the random cavity parameters  $\omega_c$  and  $\kappa_{\text{ex}}$ , and the random number seed used to generate  $\vec{W}^i$  for diffusion processes are stored for later use. The semiclassical trajectory  $\vec{r}_j(t)$  can be fully reconstructed from these parameters. The time coordinate is shifted so that the trigger event occurs at  $t = 0$ . This process is repeated to acquire  $N$  triggered trajectories.

Cavity output functions such as the experimentally measurable transmission  $T_{\text{exp}}(t, \mathcal{P})$  for each simulation parameter set  $\mathcal{P}$  are calculated from the set of trajectories  $\{\vec{r}_j(t)\}$ :

$$T_{\text{exp}}(t, \mathcal{P}) = \frac{1}{N} \sum_j^N T(\vec{r}_j(t), \mathcal{P}). \quad (6.11)$$

Reflection coefficients  $R_{\text{exp}}(t, \mathcal{P})$  are calculated similarly. Spectra are calculated by averaging output powers over a time window  $t_1 < t < t_2$  for each probe frequency  $\omega_p$ . The times  $t_1$  and  $t_2$  are chosen to be the same as in our experiments, which are typically  $t_1 = 250$  ns and  $t_2 = 750$  ns. The set of triggered trajectories  $\{\vec{r}_j(t)\}$  is valid for a given set of conditions  $\mathcal{P}$  and detection criteria  $\{C_{\text{th}}, \Delta t_{\text{th}}\}$  until the trigger at  $t = 0$ . In experiments, the probe frequency  $\omega_p$  can be changed in power and detuning upon FPGA trigger. Although the same set of trajectories is valid before  $t = 0$  for each detuning, the trajectory set must be recalculated for  $t > 0$  for each probe detuning to mimic experimental conditions for spectral measurements. A numerical solution of the master equation in a number state basis is used for calculation of  $T(t)$  in (6.11); the linearized model is only used to calculate the trajectory  $\vec{r}(t)$  and efficiently generate triggers.

Whereas experiments give access only to ensemble averaged output functions, simulations contain the full trajectory paths. Provided that the simulation offers a reasonable approximation of the true ensemble of trajectories, then these results provide a window into the atomic dynamics underlying the cQED measurement of falling atoms which are not readily clear from observations.

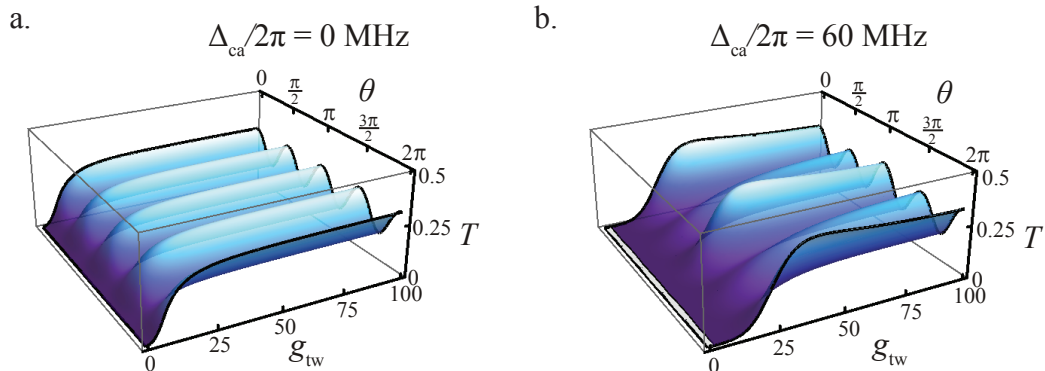


Figure 6.4: **Plots of  $T(g_{\text{tw}}, \theta, \mathcal{P})$  for (a)  $\Delta_{\text{ca}}/2\pi = 0$  MHz, and (b)  $\Delta_{\text{ca}}/2\pi = 60$  MHz, calculated numerically from (3.13).** Atoms with higher  $g_{\text{tw}}$  generally have higher  $T$  and a larger probability for detection. The variation of  $T$  with  $\theta$  is evident, with a different periodicity for the two cavity detunings.

### 6.2.5.2 Simulation distributions

The experimentally measurable cavity transmission  $T_{\text{exp}}(t)$  is obtained in (6.11) as an average over the trajectory set  $\{\vec{r}_j(t)\}$  at each time  $t$ . Eq. (6.11) can formally be written as an integration over the probability distribution of coupling constants at time  $t$ ,  $p_t(g, \theta)$ , for the given experimental parameters  $\mathcal{P}$ :

$$T_{\text{exp}}(t, \mathcal{P}) = \int dg d\theta T(g, \theta, \mathcal{P}) p_t(g, \theta). \quad (6.12)$$

The function  $T(g, \theta, \mathcal{P})$  is shown in Fig. 6.4 for the parameters  $\mathcal{P}$  relevant to experiments, specifically with  $\Delta_{\text{ca}}/2\pi = 0, 60$  MHz. For this discussion, we assume all frequencies are fixed and neglect surface shifts. In this perspective,  $T_{\text{exp}}(t)$  is not directly related to the trajectory set  $\{\vec{r}_j(t)\}$  but rather the probability distribution  $p_t(g, \theta)$  at time  $t$ . The time dependence of  $p_t$  evolves based on the underlying trajectory ensemble.

It is instructive to consider the probability distribution  $p_t(g, \theta)$  in more detail since it is the formal output of the simulations. We consider only the distribution  $p_{t=0}(g)$  over the coupling parameter  $g$  at the trigger time  $t = 0$  by integrating out the angular dependence. Through a reasonably simple analytic model (detailed in Sec. 6.2.7), we calculate  $p_{t=0}(g)$  and compare to the results of the semiclassical simulation, which includes dipole and surface forces (Fig. 6.5). For a cavity on resonance with the atom transition,  $\Delta_{\text{ca}}/2\pi = 0$ , the analytic model agrees well with a simulation when dipole and surface forces are not included. In this case, atom trajectories are nearly straight and vertical near the toroid, and the approximations of Section 6.2.7 are sufficient. When the full forces are included in the semiclassical model, the additional forces shift the distribution toward lower  $g$ . This effect is more significant for  $\Delta_{\text{ca}}/2\pi = 60$  MHz. The corresponding experimental

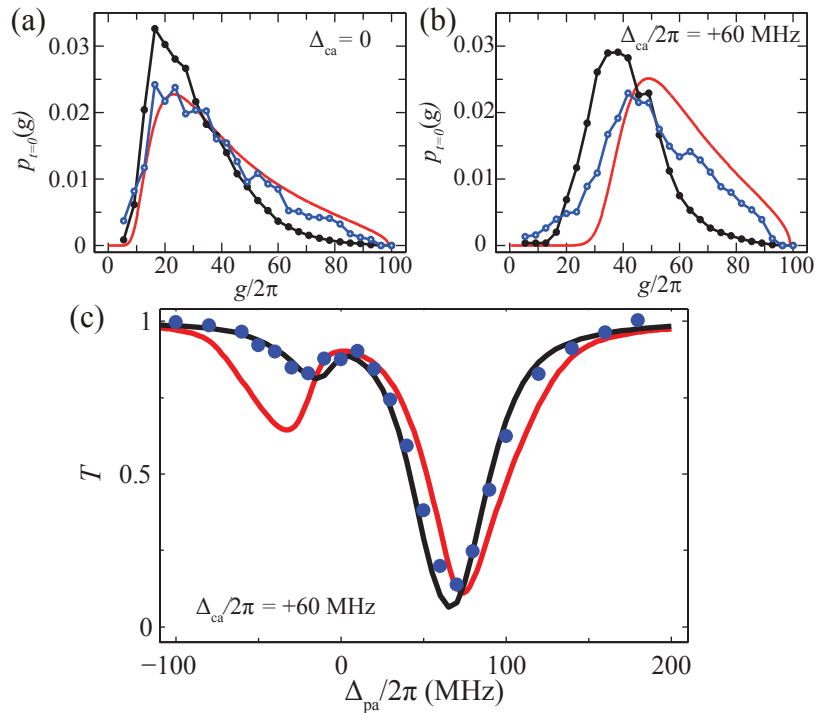


Figure 6.5: **Distributions  $p_{t=0}(g)$  of coupling constants calculated for (a)  $\Delta_{ca}/2\pi = 0$  and (b)  $\Delta_{ca}/2\pi = +60$  MHz.** Distributions from the analytic model (red), semiclassical trajectory simulation with no dipole or surface forces (blue), and the simulation with all forces (black) are shown for comparison. (c) Experimental cQED spectra data for cavity detuning  $\Delta_{ca}/2\pi = 60$  MHz (blue points) from [5] plotted with model spectra calculated from the distributions  $p_{t=0}(g)$  in panel (b). The red is the analytic model of Section 6.2.7 and black is the semiclassical simulation.

cQED spectra confirm that the semiclassical model with dipole and surface forces is necessary to reproduce spectral features in the real-time experiments (Fig. 6.5c). The overall simulation accuracy for the calculations in Fig. 6.5c is at the level of 20% in the difference between the atom and no-atom spectra. The refinements introduced to the linearized semiclassical model such as velocity-dependent forces, curvature corrections to the surface forces, and distance dependent decay rates are at a level comparable to the widths of the lines for the curves drawn in the figures.

The cavity transmission  $T$  varies as a function of the atomic azimuthal coordinate  $\theta = m\phi$ , as evident in Fig. 6.4. This biases atomic detection towards specific locations around the toroid and leads to a non-uniform angular distribution  $p_{t=0}(\theta)$  for atom location at detection. Fig. 6.6 shows distributions of the atomic angular coordinate at the detection trigger  $t = 0$  for three simulation conditions relevant to the experiments of [5]. Although averaged spectra do not explicitly measure the coordinate  $\theta$ , these simulations make it clear that trajectories passing through certain regions around the toroid are preferentially detected. The phase of the cavity output field depends on  $\theta$ , suggesting the possibility for future experiments to measure the distribution of Fig. 6.6.

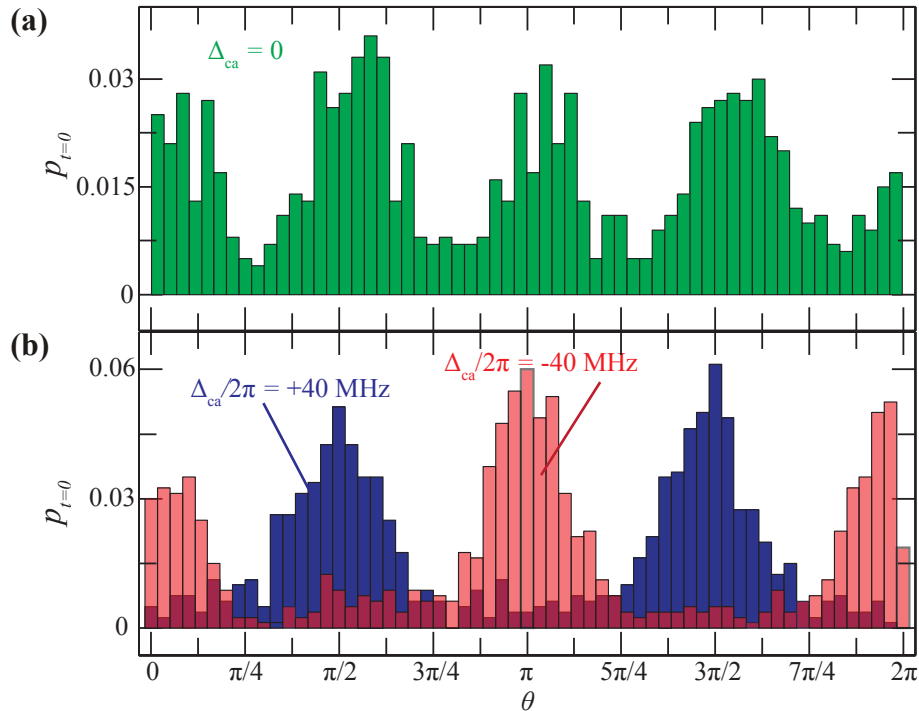


Figure 6.6: **Probability distribution  $p_{t=0}(\theta)$  of atomic azimuthal angle  $\theta = m\phi \bmod 2\pi$  at transit detection time  $t = 0$  presented as histograms of simulation runs.** Shown are the cases for cavity detunings (a)  $\Delta_{\text{ca}} = 0$  (green) and (b)  $\Delta_{\text{ca}}/2\pi = +40$  MHz (blue) and  $\Delta_{\text{ca}}/2\pi = -40$  MHz (red, semi-transparent). Normalization is such that the sum across all  $\theta$  is unity.

### 6.2.5.3 Simulated trajectories

We now turn to the simulated trajectories  $\{\vec{r}_j(t)\}$ . In contrast to experiments, in simulations we have the capability of turning certain forces selectively on and off. In particular, we can adjust the surface potential  $U_s$  and the dipole forces, referred to symbolically as  $U_d$  (despite them not being strictly derivable from a potential). To investigate the effects these optical phenomena have on atomic trajectories, we run simulations for four cases: the full semiclassical model, the model without surface forces ( $U_s = 0$ ), the model without dipole forces ( $U_d = 0$ ), and the model without any radiative forces ( $U_d = U_s = 0$ ).

Considering conditions relevant to [5], we plot simulations for two sets of experimental parameters  $\mathcal{P}_{1,2}$  in Fig. 6.7. For  $\mathcal{P}_1$ , the cavity is detuned to the red, whereas the cavity is blue-detuned in  $\mathcal{P}_2$  ( $\Delta_{\text{ca}}/2\pi = -40$  MHz for  $\mathcal{P}_1$  and  $+40$  MHz for  $\mathcal{P}_2$ ). In each set of conditions, the probe field is on resonance with the cavity for high signal-to-noise atom detection ( $\Delta_{\text{cp}} = 0$ ) and the average bare-cavity mode population of  $a$  is  $\approx 0.05$  photons. The toroid cavity parameters are those of [5],  $\{g_{\text{max}}, h, \kappa_{\text{in}}, \kappa_{\text{ex}}\}/2\pi = \{100, 11, 13, 17\}$  MHz. Comparing the full model, we see that trajectories for  $\mathcal{P}_1$  primarily crash into the surface, whereas those from  $\mathcal{P}_2$  both crash and are repelled from

the toroid. This asymmetry is due to the repulsive or attractive dipole force for different probe detunings relative to the atomic transition. The largest effect of turning surface forces *off* is seen in the blue-detuned trajectories, which have a lower crash rate when  $U_s = 0$ . With  $U_d = 0$ , both  $\mathcal{P}_1$  and  $\mathcal{P}_2$  trajectories look nominally the same; the detuning  $\Delta_{ca}$  only affects cQED spectra, with a minor imperceptible effect arising from CP potentials initially shifting the atomic transition either closer to (red) or further from (blue) the cavity field.

In addition to the qualitative differences in detected atom trajectories summarized here, the effects of  $U_d$  and  $U_s$  are evident in the experimental quantities  $T_{\text{exp}}(t)$  and  $R_{\text{exp}}(t)$ . Since here we focus specifically on trajectory calculations, the reader is referred to [5] for detailed comparisons of spectral and temporal simulations to experimental data. The present semiclassical simulations, reliable to a few percent for cQED spectra, are sufficiently accurate to understand the experimental results of [5] without further refinement.

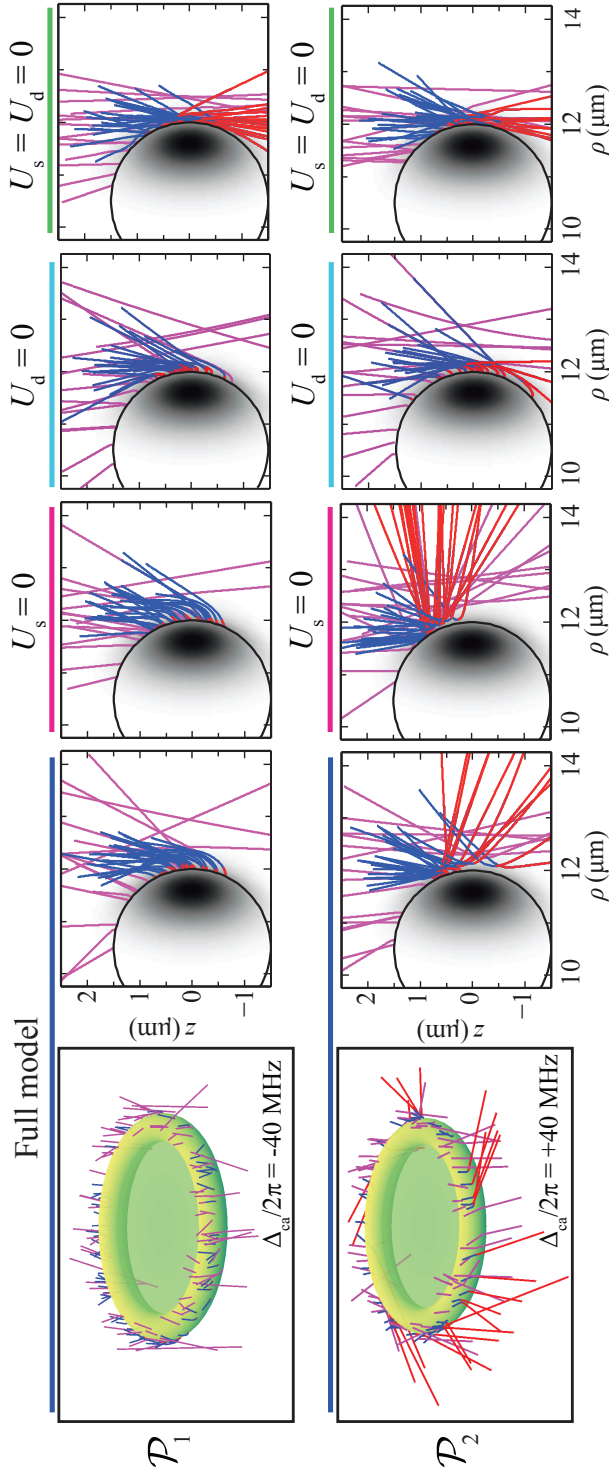


Figure 6.7: **Simulated trajectories for model parameters  $\mathcal{P}_{1,2}$  ( $\Delta_{\text{ca}}/2\pi = 40$  MHz) plotted for four models of radiative forces: the full semiclassical model,  $U_s = 0$ ,  $U_d = 0$ , and  $U_s = U_d = 0$ .** For the full model, a three-dimensional representation is shown, while trajectories are projected onto the two-dimensional  $\rho - z$  plane for all conditions. Magenta trajectories represent *un-triggered* atoms, blue paths are detected atoms for  $t < 0$  and red paths represent atom trajectories after the trigger for  $t > 0$ .

### 6.2.6 Calculating the polarizability and dielectric response functions

Evaluation of Casimir-Polder interactions of atoms with the surface of the dielectric resonator requires evaluation of the atomic polarizability and of the dielectric function as functions of a complex frequency. Here we outline our analytic model of the complex dielectric function for SiO<sub>2</sub> and the atomic polarizability of cesium atoms in the ground and excited states.

The complex dielectric function  $\epsilon(\omega) = \epsilon_1 + i\epsilon_2$  is modeled using a Lorentz oscillator model of the real and imaginary parts of the response function to analytically introduce frequency dependence and enforce causality,

$$\epsilon(\omega) = \epsilon_\infty + \sum_j \frac{f_j}{(\omega_j^2 - \omega^2)^2 + \omega^2 \gamma_j^2} ((\omega_j^2 - \omega^2) + i\omega\gamma_j). \quad (6.13)$$

Here,  $\omega_j$  is the resonance frequency,  $\gamma_j$  is the damping coefficient, and  $f_j$  is the oscillator strength for each oscillator in the model.  $\epsilon_\infty = \epsilon(\omega \rightarrow \infty) = 1$ .  $\epsilon$  can be expressed in terms of the complex index of refraction  $\tilde{n} = n + i\kappa$  as  $\epsilon = \tilde{n}^2 = n^2 - \kappa^2 + 2in\kappa$ , where  $n$  is the refractive index and  $\kappa$  is the extinction coefficient. Experimental data for  $\tilde{n}$  for SiO<sub>2</sub> is available over a wide frequency range [185], which is used to fit the parameters of (6.13) for a seven-oscillator model ( $j = 1 - 7$ ). Using the analytic form of (6.13), the dielectric function can readily be evaluated over complex frequencies as shown in Fig. 6.2.

The frequency-dependent atomic polarizability  $\alpha_s(\omega)$  for cesium in a state  $s$  is calculated as a sum over transitions of the form,

$$\alpha_s(\omega) = \sum_n \frac{e^2 f_{ns}}{m_e} \frac{1}{\omega_{ns}^2 - \omega^2}, \quad (6.14)$$

where  $e$  is the electron charge,  $m_e$  is the electron mass,  $\omega_{ns}$  is the transition frequency, and  $f_{ns}$  is the signed oscillator strength for the transition of state  $n$  to the state  $s$  ( $f_{ns} > 0$  if state  $n$  is above  $s$  in energy). A more complete expression for the response function  $\alpha(\omega)$  should include damping coefficients given by the transition linewidths. Since our calculations involve integrals over infinite frequency on the imaginary axis and atomic linewidths are generally narrow with respect to transition frequencies, we assume that the off-resonant form given by (6.14) without damping is sufficient. We also note that this expression does not account for the differences between magnetic sublevels and hyperfine splitting, which again represent small corrections when these expressions are integrated over the imaginary frequency axis. The general form of (6.14) applies to the polarizabilities for both the  $6S_{1/2}$  ground state and the  $6P_{3/2}$  excited state, with an additional tensor polarizability for the

$6P_{3/2}$  state.

The total atomic polarizability is composed of contributions from valence electron transitions ( $\alpha_v$ ) and high-energy electron transitions from the core shells to the continuum ( $\alpha_c$ ), such that  $\alpha = \alpha_v + \alpha_c$ . The valence polarizability  $\alpha_v$  constitutes 96% of the total static polarizability [59] in Cs, with  $\alpha_c$  only significant at high frequencies. We take  $\alpha_c$  to be the same for both the ground and excited states of Cs, whereas  $\alpha_v$  is obviously sensitive to the different electronic transition manifolds for the  $6S_{1/2}$  and  $6P_{3/2}$  states. Valence electron oscillator strengths and transition frequencies are tabulated in many sources [174, 145]. Our estimate of  $\alpha_v(\omega)$  for the ground state includes all  $6S_{1/2} \rightarrow NP_{1/2}$  and  $6S_{1/2} \rightarrow NP_{3/2}$  transitions, with  $N = 6 - 11$ . For the excited state,  $\alpha_v(\omega)$  is calculated using  $6P_{3/2} \rightarrow (6 - 15)S_{1/2}$ ,  $6P_{3/2} \rightarrow (5 - 11)D_{3/2}$ , and  $6P_{3/2} \rightarrow (5 - 11)D_{5/2}$  transitions. Tensor polarizability contributions sum to zero when averaged over all angular momentum sublevels [127]. In agreement with [59], our calculation of  $\alpha_v$  comprises about 95% of the total static polarizability.

For simplicity, all core electron transitions are lumped into a single high-frequency term of the form used in (6.14). This term contains two free parameters,  $f_{\text{core}}$  and  $\omega_{\text{core}}$ , which are found from the following two conditions. Using the calculation of  $\alpha_v(\omega)$  for the Cs ground state, we enforce that the ground state static polarizability  $\alpha(\omega \rightarrow 0)$  matches the known value calculated theoretically [6]  $\alpha(0) = 5.942 \times 10^{-23} \text{ cm}^3$ . We also ensure that the ground state LJ constant for a Cs atom near a metallic surface agrees with the known value [59, 117]  $C_3 = -\frac{\hbar}{4\pi d^3} \int_0^\infty \alpha(i\xi) d\xi = 4.4 \cdot h \text{ kHz } \mu\text{m}^3$ . These conditions are sufficient to fix the two free parameters in  $\alpha_c(\omega)$  for this single oscillator core model, although the high-frequency structure of the core polarizability is lost. For the excited state calculation, we use the same  $\alpha_c(\omega)$ .

### 6.2.7 Analytic model of falling atom detection distributions

Here we develop an analytic model of the distribution  $p_{\text{fall}}(g, \theta)$  of coupling parameters  $g$  and azimuthal coordinate  $\theta = m\phi$ . Atoms are assumed to fall at constant vertical velocity with no forces, in contrast to the more complete semiclassical trajectories used in this chapter to generate  $p_t(g)$ . An abbreviated description of this model is discussed in Sec. 5.10.1.

The linearized steady-state cavity transmission  $T(\Delta_{\text{ap}}, g(\vec{r}))$  is a known function of  $\Delta_{\text{ap}}$  and  $\vec{r}$ . We only consider the lowest order mode where the cavity mode function is approximately Gaussian in  $z$  and exponential in distance from the surface  $d$ . The approximate temporal behavior of the

coupling constant  $g$  for a single trajectory is,

$$g(\rho, z(t)) = g_c(\rho)e^{-(z(t)/z_0)^2}, \quad (6.15)$$

where  $g_c(\rho)$  is the maximum value of the  $g$  at the closest approach of its trajectory ( $z = 0$ ),  $z_0$  is a characteristic width assumed to be independent of  $\rho$ , and  $z(t) = -vt$ .  $g_c(\rho)$  decays exponentially from the maximum  $g_{\max}$  at the toroid surface,  $g_c(\rho) \sim g_{\max}e^{-(\rho-D_p)/\lambda_0}$ . The transmission  $T$  and hence the detection probability depend on  $\theta$ ; in general, if atoms fall uniformly around the toroid, the most numerous trajectories detected will be at the values of  $\theta$  which maximize  $T(\theta)$  for the cavity parameters of interest ( $\theta = \pi/2$  for  $\Delta_{\text{ca}}/2\pi = +40$  MHz, for example, as in Fig. 6.6).

The probability density function for the full ensemble of detected falling atoms  $p_{\text{fall}}(g, \theta)$  can be estimated as the product of the probability of any atom having a particular  $g$  and the probability of a trigger event occurring for an atom with coupling  $g$ ,

$$p_{\text{fall}}(g, \theta) \sim p_{\text{atom}}(g)p_{\text{trigger}}(g, \theta). \quad (6.16)$$

An atom transit is triggered when the total detected photon counts exceeds a threshold number,  $C_{\text{th}}$ , within a detection time window  $\Delta t_{\text{th}}$ . For a probe beam of input flux  $P_{\text{in}}$ , the mean counts in this window are  $\bar{C} = T(g, \theta)P_{\text{in}}\Delta t_{\text{th}}$ . This expression assumes that the atom is moving slowly so that the  $T(g, \theta)$  at the trigger event is the only  $T(g, \theta)$  that contributes to the detection probability. The detection probability  $p_{\text{trigger}}(g, \theta)$  is estimated from a Poisson distribution of mean count  $\bar{C}$ .

From (6.15),  $p_{\text{atom}}(g)$  can be written as a product of the probability  $p(g|g_c)$  of an atom in a trajectory with a given  $g_c$  to have coupling  $g$  and the probability of a trajectory to have that  $g_c$ ,  $p_{\max}(g_c)$ , integrated over all  $g_c$ ,

$$p_{\text{atom}}(g) = \int_g^{g_{\max}} p(g|g_c)p_{\max}(g_c) dg_c. \quad (6.17)$$

The integral has limits from  $g$  to  $g_{\max}$  since  $g_c$  cannot be smaller than  $g$ .

For atoms falling uniformly over the  $\rho - \phi$  plane,  $p_{\max}(g_c) dg_c$  is proportional to the area of a ring of radius  $\rho$  and thickness  $d\rho$ ,  $p_{\max}(g_c) dg_c \sim 2\pi\rho d\rho$ . Using  $g_c(\rho) \sim e^{-(\rho-D_p/2)/\lambda_0}$ ,  $\frac{dg_c}{g_c} \sim -\frac{d\rho}{\lambda_0}$ . Hence,  $p_{\max}(g_c) \sim 1/g_c$  for  $(\rho - D_p/2) \ll D_p/2$ . To find  $p(g|g_c)$  we note that the probability is proportional to the time an atom in the trajectory is at a particular  $g$ . From (6.15) for a constant velocity  $v$ , this trajectory is Gaussian and the relative probability must be proportional to  $dz$ .

Finding the differential as a function of  $g$  gives  $p(g|g_c) \propto dz \sim \frac{1}{g\sqrt{\ln(g_c/g)}}$ .

Putting the results together in (6.17) gives

$$p_{\text{atom}}(g) \sim \int_g^{g_{\text{max}}} \frac{1}{gg_c} \frac{dg_c}{\sqrt{\ln(g_c/g)}} \sim \frac{\sqrt{\ln\left(\frac{g_{\text{max}}}{g}\right)}}{g}. \quad (6.18)$$

This result diverges as  $g$  goes to zero since there are infinite transits with small  $g_c$  and infinite time for atoms with small  $g$  for any transit regardless of  $g_c$  for  $t \rightarrow \pm\infty$ . This divergence is not problematic in calculating (6.16) since  $p_{\text{trigger}}(g, \theta)$  cuts off for low  $g$  faster than the logarithmic divergence in  $p_{\text{atom}}(g)$ .

The spectrum for given experimental parameters as a function of probe detuning  $\Delta_{\text{ap}} = \omega_p - \omega_a^{(0)}$  can be written as:

$$T(\Delta_{\text{ap}}) = \int_0^{g_{\text{max}}} T(\Delta_{\text{ap}}, g, \theta) p_{\text{fall}}(g, \theta) dg d\theta, \quad (6.19)$$

where the normalization of  $p_{\text{fall}}(g, \theta)$  is chosen such that

$$\int_0^{g_{\text{max}}} p_{\text{fall}}(g, \theta) dg d\theta = 1. \quad (6.20)$$

The overall probability of  $g$ ,  $p_{\text{fall}}(g)$  independent of  $\theta$ , is found by integrating over  $\theta$ . In practice,  $p_{\text{fall}}(g)$  is quite similar to  $p_{\text{fall}}(g, \theta)$  evaluated for the  $\theta$  which maximizes the transmission. Fig. 6.5 compares this simple model for  $p_{\text{fall}}(g)$  with the equivalent distribution from the semiclassical trajectory simulation,  $p_{t=0}(g)$ .

### 6.3 Trapping of atoms near dielectric surfaces

In Chapters 4 and 5, we discuss the realizations of strong coupling between falling single cesium atoms and a microtoroidal resonator, with interaction times of a few microseconds. Despite this advance in monolithic resonator chip-based cavity QED, the short interaction time presents a limiting factor, for example in single-shot measurement signal-to-noise ratio, processing or storage times for quantum information protocols, and in integration for the realization of a multi-nodes entanglement/functioning quantum network (which requires multiple nodes to have strongly coupled trapped atoms at the same time). In addition, it also allows exploration of other types of physics including many-body quantum dynamics, high precision surface-atom effect measurements, and in the case of orbiting traps, investigation of angular dynamics.

Realizations of strong coupling cavity QED with trapped atoms using nanophotonic devices will open up multiple exciting possibilities. In this section, we discuss several schemes that may lead to the realization of an optical trap for single atoms using an on-chip microtoroidal resonator.

### 6.3.1 Optical tweezer trap

A potentially promising scheme to trap single atoms next to a microtoroidal resonator is to use a common technique of optical tweezer dipole trap with red-detuned focused beam that provides three dimensional confinement for a single atom close to a microtoroid’s surface. While an optical tweezer trap for a single atom has been realized at a sub-micron scale, using diffraction-limited focused FORT beam with numerical aperture of 0.7 formed by multiple lenses with a 1 cm working distance [211] (more recently, [234]), there are a number of physical and practical limitations present in this approach.

Firstly, scalability and integrability may require miniaturization of the imaging system used to form the tightly focused beam. In the microtoroid lab in our group, we (particularly Scott Kelber and Cindy Regal) investigated an approach to this issue by using a lensed-fiber (from Nanonics Imaging) that creates a tightly focused beam with numerical aperture of 0.7 (beam radius of 300 nm) with a working distance of 5  $\mu\text{m}$ .

Secondly, in general the diffraction limit imposes a minimum distance an atom trap can be located relative to the surface of the toroid of  $\approx \lambda_{\text{dip}}/2$ , which is larger than the  $1/e$  decay length of the microtoroid’s whispering-gallery-mode evanescent field of  $\lambda/2\pi \approx 136$  nm for  $\lambda = 852$  nm. Although this is true in general, there are potential solutions that can reduce the trap-to-toroid distance significantly. For example, reflecting the FORT beam off the toroid’s surface at normal incident could generate a standing-wave pattern with first local intensity maximum located at  $\lambda/4$  from the toroid’s surface (e.g., for  $\lambda_{\text{dip}} \gtrsim 852\text{nm}$ , it is  $\gtrsim 213$  nm). Another potential solution is to use self-imaging nanoscale patterns that may be implemented onto the lensed-fiber tip, a technique that has been demonstrated in a different system [119] where local intensity maxima with  $< \lambda/4$  sizes have been realized.

Thirdly, the positioning of the trap location with respect to the on-chip toroid presents a practical limitation. Here, the optical beam size and working distance of the focusing lens present geometrical constraints.

Finally, assuming the tweezer trap does not get ‘destroyed’ by the presence of the silica toroid (which preliminary analysis showed may be the case for the system considered), then there is the

challenge of atom loading into the conservative optical tweezer trap.

As the toroid is fabricated on top of an opaque silicon chip substrate, realization of atom cooling near a microtoroid is challenging, as we have limited optical access. This is in contrast for example with the nanofiber trap discussed in Sec. 3.2, where one could overlap a magneto-optically trapped cloud of cold atoms in an optical molasses with the nanophotonic nanofiber device. A potential solution is to utilize multiple optical conveyor belts discussed in Sec. 3.1.2.1, which may require additional optical components such as additional lensed fibers. Another potential solution is investigated in a recent experiment [235], using Raman sideband cooling combined with the application of a magnetic bias field to mitigate effects from polarization ellipticities formed by the tightly focused light (with significant longitudinal polarizations as discussed in Sec. 2.5). Here, an optical tweezer trap is demonstrated by using a focusing lens with a numerical aperture of 0.43, where atoms are loaded from a magneto-optical trap. Transport over a distance of  $\approx 20 \mu\text{m}$  is also demonstrated by using a scanning galvanometer mirror [235].

In conclusion, these schemes offer promising potential to be candidates for single atom trapping near a microtoroid cavity. There are potential solutions that may be implemented to allow toroid-to-trap distances comparable to the decay lengths of the toroid's evanescent field. There are however quite a number of practical challenges such as in the loading process and position control that may post significant limitations in terms of scalability and on-chip integrability.

## 6.3.2 Orbiting trap

### 6.3.2.1 Trapping atoms in the evanescent field of a microtoroid

Our trajectory simulation discussed in Sec. 6.2 can be extended to study trapping of atoms in a two-color evanescent far off-resonant trap (eFORT) near a microtoroidal resonator [5, 228]. An evanescent field trap takes advantage of the wavelength dependence of scale lengths for the optical dipole force of two optical fields with frequencies far-detuned from the atomic transition to limit scattering [52, 179, 69]. The relative powers of the two fields are set so that near the surface, the blue-detuned, repulsive field is stronger than a red-detuned attractive field. As each field falls off with a decay constant of roughly  $\lambda = 2\pi/\lambda$ , at some distance the red, attractive field will dominate and the atom will be attracted to the surface forming a potential minimum. Recently, evanescent fields have been harnessed to trap atoms in a two-color eFORT around a tapered optical fiber [248], where the fiber enables efficient optical access to deliver both high intensity trapping fields and weaker probe fields to the trapped atoms in a single structure. The tapered fiber can be positioned

as desired, bringing the trapped atoms near a device for atomic coupling.

The tapered nanofiber eFORT is a remarkable achievement toward integrating atom traps with solid-state resonators, but the nanofiber scheme does not allow direct integration with a cavity for achieving strong, coherent coupling between light and trapped atoms. Another disadvantage is that trap depth is limited by the large total power required to achieve trapping with evanescent fields. The high quality factors and monolithic structure of WGM resonators allow evanescent field traps free from these problems while maintaining efficient optical access from tapered fiber coupling. Two-color evanescent field traps in WGM resonators have been analyzed in detail for spheres [246] and microdisks [201]. In this section, we extend our simulations of atoms in the evanescent field of a microtoroid to an eFORT that can capture single falling Cs atoms triggered upon an atom detection event.

Unlike nanofibers, a microtoroid cannot be placed directly in a magneto-optical trap for a source of cold atoms. As shown in [5], we have the experimental capability to detect a single atom falling by a microtoroid and trigger optical fields while that atom remains coupled to the cavity mode. The semiclassical simulations described here are ideal for investigating the capture of falling atoms in a trap triggered upon experimental atom detection.

We add an additional eFORT potential  $U_t$  to our semiclassical trajectory model in addition to the dipole forces and surface potential  $U_s$ . For our simulation,  $U_t$  is formed from a red (blue)-detuned mode near 898 nm (848 nm) with powers  $\sim 50 \mu\text{W}$  to give a trap depth of  $\sim 1.5 \text{ mK}$  at  $d \sim 150 \text{ nm}$  from the surface (Fig. 6.8a). The red (blue) fields interact primarily with the  $6S_{1/2} \rightarrow 6P_{1/2}$  ( $6S_{1/2} \rightarrow 6P_{3/2}$ ) transition. The trap depth is limited by the total power in vacuum that can propagate in the tapered fibers of [5]. Power handling can be improved with specific attention to taper cleanliness, so with experimental care the trap depth can be increased reasonably from the discussion here, although we simulate under the conditions given to illustrate that this trap is already experimentally accessible.

The difference in vertical scale lengths ( $\psi_0$  in (3.3)) for modes of different wavelength leads to a trap that is not fully confined if both the red- and blue-detuned trap modes are of the lowest order (as in Fig. 3.1.1.1b). As  $|\psi|$  increases, the repulsive blue-detuned light weakens faster than the red-detuned field, and atoms can crash into the toroid surface. This problem is alleviated by exciting a higher-order mode for the 898 nm light, as shown in Fig. 6.8b. The modal pattern confines atoms near  $z = 0$  and prevents trap leakage along  $\psi$ . This problem is not present in the microdisk eFORT of [201] because the optical mode extent is determined by structural confinement and not

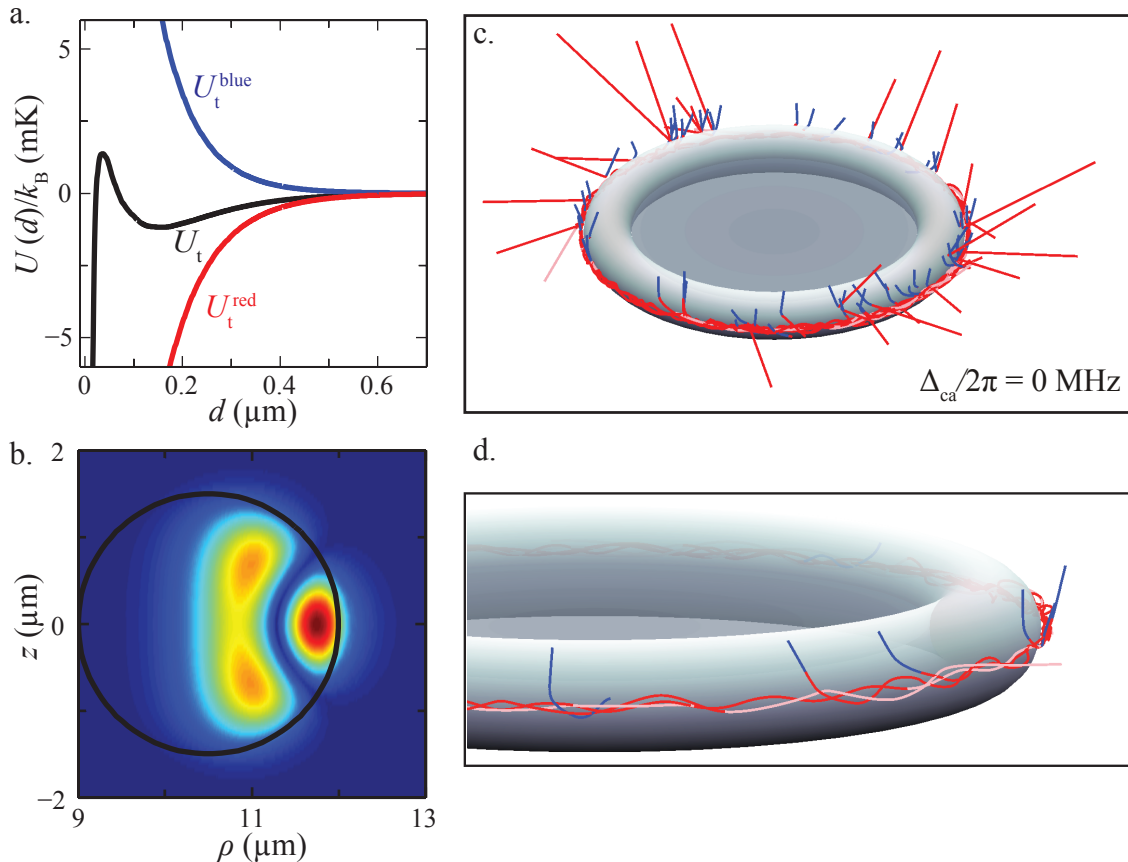


Figure 6.8: **(a)** The trapping potential  $U_t$  along the  $z = 0$  axis with the CP potential included. Also shown are the red and blue evanescent potentials of the two trapping modes,  $U_t$ , respectively. **(b)** The mode function used in  $U_t$  for the 898 nm mode with  $m = 106$ . **(c)** Simulated trajectories for trapping simulations with an eFORT  $U_t$  triggered “on” by atom detection at  $t = 0$  with  $\Delta_{\text{ca}} = 0$ . Falling atoms with the FORT beams “off” ( $t < 0$ ) are colored blue, whereas trajectories after the trap is triggered are red. Trajectories are colored pink for  $t > 50 \mu\text{s}$  to illustrate the timescale. Roughly 25% of the triggered trajectories become trapped. **(d)** Same as (c) showing only the trapped trajectories and a clearer view of atom orbits in the evanescent trap. Note: this figure appears in [228].

the optical scale length. Use of a higher-order mode was also used to form an atom-gallery in a microsphere [246].

During the detection phase of the simulation,  $U_t = 0$ . At  $t = 0$  conditioned on an atom detection trigger,  $U_t$  is turned on. The kinetic energy of an atom with typical fall velocity of  $v \sim 0.2$  m/s is equivalent to 0.3 mK, so a 1.5 mK trap is sufficiently deep to capture an atom if it is triggered near the trap potential minimum. Defining a trapped trajectory to be one such that the atom has  $g/2\pi > 5$  MHz at  $t = 10 \mu\text{s}$ , approximately 25% of triggered atom trajectories are captured when the trapping potential is turned on. Simulated trapping times exceed  $50 \mu\text{s}$ , limited not by heating from trapping light but by the radiation pressure from the unbalanced traveling whispering-gallery

modes of a nearly-resonant optical probe field. This probe field can be turned off so that the atoms remain trapped beyond the simulation time.

In contrast to the standing-wave structure of a typical eFORT or Fabry-Perot cavity trap [259], microtoroidal resonators offer the tantalizing possibility of radially confining an atom in a circular orbit around the toroid [246, 158]. The  $U_t = 0$  outlined here does not confine the atoms azimuthally, forming circular atom-gallery orbits around the microtoroid [158] (Fig. 6.8c,d). In the same manner as [248], a localized trap can be achieved by exciting a red-detuned standing wave for three-dimensional trap confinement.

This trapping simulation outlines how real-time atom detection can be utilized to trap a falling atom in a microtoroidal eFORT. In practice, microtoroidal traps present some serious practical challenges. Notably, because the trap quality is sensitive to the particular whispering-gallery mode, the excited optical mode must be experimentally controlled. The success of an eFORT for Cs atoms around a tapered nanofiber [248] strongly suggests that similar trap performance might be achieved for an eFORT around a high- $Q$  WGM cavity, localizing atoms in a region of strong coupling to a microresonator.

### 6.3.2.2 Microtoroidal cavity modes, spectrum and tunability

In the previous section, we discuss a scheme to trap single atoms in orbit around a microtoroid via evanescent field FORT trap. One challenging capability required to realize such a trap is the ability to excite particularly chosen higher order modes of a toroid. As discussed previously, there are a number of factors that limit the intrinsic  $Q$  (or the intrinsic loss rates) of a microtoroidal cavity, including bulk material absorption, surface contaminant and surface scattering, and radiation loss. For a silica microtoroid with a relatively small size relevant to the work in this thesis (e.g., with diameter  $\ll 100 \mu\text{m}$ ), the  $Q$  is limited not by bulk material absorption of silica ( $Q_{\text{bulk}} \sim 10^{10}$ ), nor radiation losses ( $Q_{\text{rad}} > 10^{13}$ ), but the limiting factor is the absorption by surface contaminants such as OH and water molecules, and surface scattering losses [224, 134, 261]. Because of this, the total quality factor  $Q$  of a microtoroidal cavity is sensitive to the amount of electric field that is present at the surface boundary of the toroid, leading to the tendency for the fundamental mode to have a higher  $Q$  than the higher order modes. Empirically, we regularly observe a spectrum or ‘forest’ of many (10-100) cavity resonance frequencies over a frequency scan range of 5-10 nm (roughly a free-spectral-range) of a toroid. Most of these resonances have  $Q$  that are a few orders of magnitude lower than the ‘maximum’ good  $Q$  that we utilize, of  $Q \sim 10^7$ , for our geometry ( $D_p = 10\text{-}20 \mu\text{m}$ ,

$D_m = 3\text{-}6\ \mu\text{m}$ ,  $\lambda \approx 852\ \text{nm}$ ). This cavity resonance  $Q$  signature provides a guide for us to excite the fundamental mode of the toroid<sup>1</sup>. The excitation of higher-order modes, however, is quite different and more challenging.

Figure 6.9 a) shows cross-sectional  $|E|$  profiles of a microtoroid's whispering-gallery mode from the fundamental  $z$ -polarized mode (labeled 1) and  $\rho$ -polarized mode (labeled 1'), to the 6th-order modes, labeled by the number  $n$  for  $n$ -th order mode, with unprimed numbers indicating  $z$ -polarized modes and primed numbers indicating  $\rho$ -polarized mode. Fig. 6.9 b) shows the corresponding spectrum (resonance frequencies) for azimuthal mode numbers of  $m = 117, 118, 119$ . For our microtoroid cavity QED experiment system considered in Chapter 5 and Sec. 6.2, we have  $m = 118$ , toroid principal diameter  $D_p = 12\ \mu\text{m}$ , minor diameter of  $D_m = 3\ \mu\text{m}$ , with fundamental mode polarized in  $z$  (labeled 1 in part a) of the figure). This mode is temperature-tuned (base temperature  $\approx 100\ \text{°C}$ ) to cesium D2 line shown in Fig. 6.9 b) as the dashed vertical line, more specifically to the  $F=4 \rightarrow F'=5$  transition. The numbers 1 to 10 next to the blue lines refer to the fundamental (1st order) to 10th order modes, with the primed numbers always subsequent to the unprimed numbers. These lines of resonance frequencies of the microtoroid mode are calculated using Comsol. Note that we do not take into account the finite linewidths of the cavity modes, we only show the lines representing the resonant frequencies of the cavity modes.

Now recall that as discussed in Sec. 6.3.2.1, we considered an orbiting trap scheme that requires excitation of the fundamental mode (mode 1 or 1') for blue-detuned FORT, as well as the 3rd order mode (mode 3 or 3') for the red-detuned FORT, in order to form a fully closed trap potential. While this may seem like a simple task, it requires the ability to excite particular high-order modes of the microtoroid. Now, the free-spectral-range of the toroid for our typical experimental parameters ( $D_p = 12\ \mu\text{m}$ ,  $D_M = 10.5\ \mu\text{m}$ ,  $D_m = 3\ \mu\text{m}$ ,  $\lambda = 852\ \text{nm}$ ),  $\text{FSR} = 6.85\ \text{nm}$  (or in frequency units,  $2.8\ \text{THz}$ ) is significantly smaller than the differences in frequency between different modes of the toroid, as evident in Fig. 6.9 b). Because of this, the task of selecting a particular high-order mode becomes practically quite challenging, as we have to be able to pick the desired mode within a 'forest' of modes present in the structure. We note that there are potential solutions to this problem, for example by figuring out the exact spectral profiles (including variations in linewidths of each of the resonances); the frequency shift responses, which may occur at a different rate or to a different extent, in response to changing parameters such as temperature; and finally, also the possibility of performing direct

<sup>1</sup>In our experiments, we also perform other checks that support excitation of the fundamental mode, such as mapping the spatial field pattern of the toroid's excited mode by scanning the position of tapered fiber, toroid-taper optical coupling, and cavity QED analyses (i.e., atom-photon coupling strength  $g$  profile, and atom dynamics in cQED).

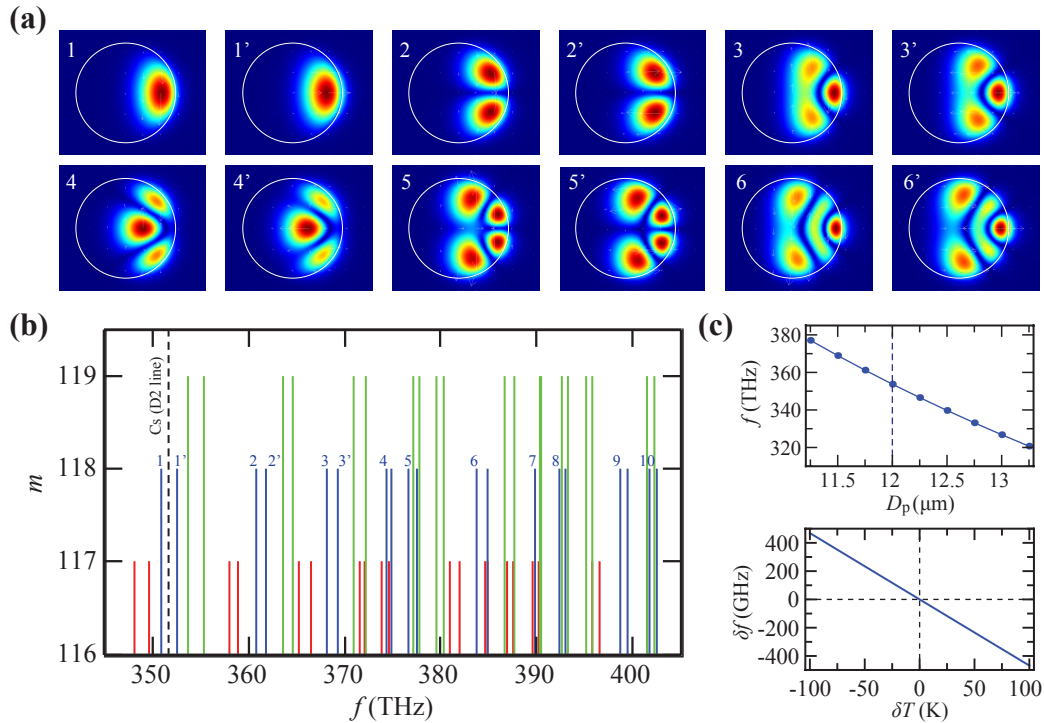


Figure 6.9: **Whispering gallery modes of a microtoroid.** **a)** Transverse cross-sectional plots showing electric field amplitude  $|E|$  for the first six modes of a silica microtoroid with principal diameter  $D_p = 24 \mu\text{m}$  and minor diameter  $D_m = 3 \mu\text{m}$ , for  $z$ -polarized (unprimed labels) and  $\rho$ -polarized (primed labels) modes. **b)** Plots of azimuthal mode number  $m$  as a function of toroid's resonance frequencies  $f$ , showing a 'forest' of modes in the spectrum, for  $m = 117$  (red),  $m = 118$  (blue), and  $m = 119$  (green). The plots in a) corresponds to  $m = 118$ . **c)** Sensitivity of resonant frequency for  $m = 118$ ,  $z$ -polarized mode (the mode used in the experiment described in Chapter 5) as a function of principal diameter  $D_p$  (for minor diameter  $D_m = 3 \mu\text{m}$ ) and temperature change  $\delta T$  in Kelvin.

near-field scanning optical microscopy (NSOM) for example by moving the tapered fiber next to the microtoroid, or using an independent probe [139, 138].

Figure 6.9 c) shows in the top panel the change in resonant frequency of the  $m = 118$ ,  $z$ -polarized fundamental-mode, as a function of varying principal diameter  $D_p$ , with the dashed line indicating the principal diameter  $D_p = 12 \mu\text{m}$  used in the calculations of parts a) and b). The points represent each of nine Comsol calculation results for the corresponding principal diameter values. The bottom panel of part c) of the figure shows the frequency response to temperature, for  $m = 118$ ,  $z$ -polarized fundamental-mode,  $D_p = 12 \mu\text{m}$ ,  $\lambda$  corresponding to the first fundamental mode labeled by the number 1 (blue line) in Fig. 6.9 c). The cavity resonance frequency response to temperature is due to two factors, namely the change in refractive index of silica, and the mechanical thermal expansion of silica, the former having much larger effect for our typical experimental parameters. More specifically, the change in cavity wavelength  $\lambda_{\text{cav}}(n, R)$ , which is a function of the refractive

index  $n$  and toroid's size or radius  $R$ , is given by [134]:

$$\frac{d}{dT}\lambda_{\text{cav}}(n, R) = \lambda_{\text{cav}}\frac{dn}{dT} + \lambda_{\text{cav}}\frac{dR}{dT}, \quad (6.21)$$

where in our case, we use  $\lambda_{\text{cav}}$  = the wavelength corresponding to the fundamental mode labeled by number 1 in Fig. 6.9 b), close to cesium line 852 nm; temperature dependence of the refractive index  $\frac{dn}{dT} = 1.28 \times 10^{-5} \text{ K}^{-1}$  for silica; and thermal expansion coefficient of silica  $\frac{dR}{dT} = \alpha = 5.5 \times 10^{-7} \text{ K}^{-1}$ . In our experiment, we use temperature tuning to tune the cavity resonance frequency to cesium transition, by using a Peltier (and thermistor in contact with the toroid chip inside the vacuum chamber) actively temperature locked at  $\approx 100^\circ\text{C}$  for base temperature, and a larger bandwidth laser heating beam focused onto the toroid chip (not very close to the toroid to avoid light leakage into the tapered fiber), which is also actively locked with a bandwidth of about 8 Hz, as we alternate between this temperature lock and running the entire experiment sequence and taking measurement data. This temperature locking method maintains the toroid's resonant frequency to within a few MHz of the cesium transition frequency.

### 6.3.3 Toroid-fiber trap

In this section we discuss a scheme to trap single atoms next to a microtoroidal cavity using a tapered optical nanofiber, which is illustrated in figure 6.10 a). In Chapter 5, we discuss a two-chamber setup connected by a differential pumping tube where an atomic cloud magneto-optically trapped in the source chamber is transported by way of an optical conveyor belt (formed by counter-propagating red-detuned FORT beams as shown in the figure by the red arrows), to the science chamber where a microtoroid chip is positioned. In this scheme, starting with this procedure, we add a mirror as shown in the figure, allowing three-dimensional polarization-gradient cooling (green arrows) to provide cooling to load the atoms into a (conservative) optical trap formed by the nanofiber (counter-propagating red and blue arrows indicating the red- and blue-detuned fiber-guided beams used to form the state-insensitive trap as will be discussed in Chapter 7). We note that metallic mirror such as gold is used to allow minimum adverse effects to the reflecting cooling beam polarizations, and the metal plate (copper) on which the microtoroid silicon chip is mounted, provides the thermal conductivity required for temperature stabilization. A top-view photograph of the experimental setup is shown on the top-left of the figure, with a tapered nanofiber that is fabricated with the same specifications as in the experiment discussed in Chapter 7 (nanofiber radius  $a = 215 \text{ nm}$ ), but without a microtoroid chip at the time of the photograph. Figure 6.10 b) shows a fluorescence signal

from an atom cloud transported from the source to science chamber, overlapped with the nanofiber in the science chamber, without trapping or cooling, pumped by a resonant beam from the direction of the green arrow labeled (i) in the figure. Lastly, as illustrated in Fig. 6.10 a), the next step of the scheme involves transporting the loaded nanofiber-trapped atoms to the vicinity of the microtoroid by employing another optical conveyor belt formed by chirping the frequency of the red-detuned standing wave FORT beams that make up the lattice potential along the nanofiber [215]. Note that stand-alone nanofiber atom traps have been realized to date; For example: in the landmark experiment of [248], and in our state-insensitive nanofiber trap experiment discussed in Chapter 7. The state-insensitivity of our trapping scheme is of a particular importance to the toroid-fiber trap scheme described in this section, as it allows the transition frequencies of the trapped atoms to remain within the cavity’s resonant linewidth, as the atoms move within the traps.

Although the abovementioned scheme seems feasible to realize, the integration of this microtoroid-fiber system presents several important challenges. Firstly, as discussed in Chapter 5, positioning of a nanofiber with respect to a microtoroid cavity requires stacks of nanopositioners to provide sufficient spatial degrees of freedom. Consequently, it is not very practical to have a dedicated nanofiber for trapping and another independent nanofiber for optical coupling into and out of the toroid. While it is possible to use just a single nanofiber serving the dual purposes of input-output optical coupling to the toroid, and atom trapping<sup>2</sup>, the positioning of the nanofiber presents a compatibility challenge that we will discuss later.

Figure 6.11 shows trap potentials using a set of ‘good’ parameters in our parameter scans, taking into account multiple aspects of the scheme, including trap potential transition as one approaches the microtoroid along the nanofiber, trap potential profile in the presence of Casimir-Polder forces near the dielectric surfaces, toroid-fiber super-mode, and atom-photon coupling strength  $g$ . Fig. 6.11 a) shows a close-up of a nanofiber next to a microtoroid, where in (i), the nanofiber is far enough from the toroid that we treat it as a stand-alone nanofiber, and in (ii), the toroid-fiber gap is at its smallest: here we treat (approximately) the toroid-fiber system as two parallel cylindrical silica waveguides with fiber radius  $a = 215$  nm, and toroid minor diameter  $D_m = 3$   $\mu$ m. At this closest approach (ii), with a surface-to-surface gap of 400 nm, the parallel waveguide composite system supports two modes polarized along the  $x$  direction, the even (symmetric) and odd (anti-symmetric) modes shown in the two columns in Fig. 6.11 c), for the red-detuned (937 nm) and blue-detuned (687 nm) magic

<sup>2</sup>Note that this involves spectral filtering of the trapping beams ( $\sim 10$  mW) to be decoupled to the probe beams ( $\sim 100$  fW) at the fiber input-output ports, requiring more than 11 orders of magnitude extinction ratio. This can be achieved by using a cascade of volume Bragg gratings providing high transmission (diffraction) efficiency at the same time. We used this in our fiber trap experiment discussed in Chapter 7.

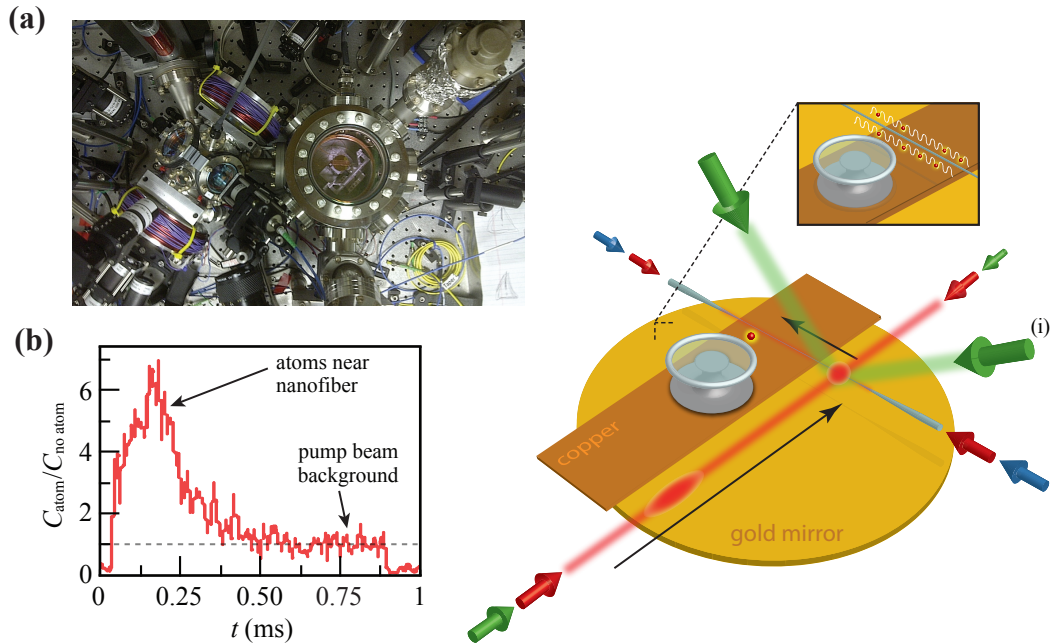


Figure 6.10: **Nanofiber atom trap and microtoroid cavity scheme.** **a)** Top view of experimental setup for atom trapping next to a microtoroidal cavity using a tapered nanofiber. Right diagram: Atom cloud transported by a free-space optical conveyor belt (one-dimensional dipole trap lattice) formed by counter-propagating red-detuned beams (red arrows), which is loaded into a nanofiber trap (formed by two pairs of red- and blue-detuned beams using our magic-compensated scheme described in Chapter 7, red and blue arrows) as it is cooled by polarization-gradient cooling beams (green arrows), and transported along the fiber by another optical conveyor belt to the toroid. The gold mirror provides reflections of the cooling beams (green arrows) in the vertical plane, and the copper plate provides thermal conductivity for cavity temperature control. **b)** Photon counts measured at the output of the fiber coming from fluorescence of atom cloud in the conveyor belt trap at the science chamber (overlapped with tapered fiber). The  $y$ -axis is the ratio of photon counts with atom and without atom,  $C_{\text{atom}}/C_{\text{noatom}}$ . A resonant pumping beam that illuminates the atom cloud and nanofiber in the cooling beam direction labeled (i) is turned on at  $t = 0.04$  ms, and turned off at  $t = 0.9$  ms.

wavelengths along the two top and bottom rows, respectively. The color of the contour plots shows the magnitude of the electric field  $|E|$ , as shown by the color bar at the bottom. In Fig 6.11 b), the  $x$  axis origin is located at the axis of the nanofiber, so that the left end of the plot corresponds to  $x_1 = a = 215$  nm, the nanofiber radius, and  $x_6 = 615$  nm is the microtoroid's surface, with 400 nm surface-to-surface gap. The thick colored trap potential curves correspond to the ground-state  $F=4$  manifold. These curve appear to overlap with the thick black dashed curves, which represent the ground-state  $F=3$  manifold. Finally, the thin colored curves represent the excited state  $F'=4$  manifold. The set of curves labeled (i) in Fig. 6.11 b) corresponds to the single-fiber (far from toroid) case as shown in (i) in Fig. 6.11 a), while the set of curves labeled (ii) corresponds to the closest approach case of the two parallel waveguide composite system. The line that appears at  $x_2$

in Fig. 6.11 b) is part of the total potential  $U$ , which includes Casimir-Polder potentials of both the fiber and toroid's dielectric surface. The line at  $x_2$  shows that the potential  $U$  rapidly decreases as  $x$  comes close to the nanofiber's surface. The Casimir-Polder (surface) potential for the fiber's surface is taken into account as the stronger van der Waals potential (limit),  $U \approx C_3/(x - a)^3$  potential, where  $a$  is the fiber radius, and  $C_3$  is the van der Waals coefficient with the value  $C_3 = 1.13 \times 10^{-48}$  mK.m<sup>3</sup> for ground-state, and  $C_3 = 7.69 \times 10^{-49}$  mK.m<sup>3</sup> for excited state. The Casimir-Polder potential near the toroid's surface is calculated with the full calculation as described in Sec. 6.2.4.2. The configuration used for this plot consists of counter-propagating red-detuned beams at  $\lambda = 937$  nm, each with a power of  $P_{\text{red}} = 0.4$  mW, and counter-propagating blue-detuned beams ( $\lambda = 937$  nm, with small  $\sim 100$  GHz detuning), each with a power of  $P_{\text{blue}} = 10$  mW.

In Fig 6.11 d), just as in part c) of the figure,  $x_1 = 215$  nm,  $x_2$  shows the rapidly decreasing van der Waals potential near the fiber surface, and  $x_6 = 615$  nm shows the surface of the toroid. The red colored trap potential curves are the same as the curves shown in part c), whereas the blue colored trap potential curves are calculated with  $P_{\text{red}} = 0.36$  mW each,  $P_{\text{blue}} = 11$  mW each (a 10% decrease and increase in the red-detuned and blue-detuned beam powers respectively), and the green colored trap potential curves correspond to  $P_{\text{red}} = 0.44$  mW each,  $P_{\text{blue}} = 9$  mW each. These different trapping beam power cases illustrate the sensitivity of the trap potential to changes in powers at the  $\approx 10\%$  level. We note that, although the ground-state trap potential is degrading but is still present as we go from green to red to blue curves, the trap potential for the excited states degrades to become anti-trap for the blue curves. These degradations are caused largely by the very strong Casimir-Polder force near the toroid's surface, forming steep potential "cliffs". While this suggests increasing of the trap-to-toroid distance, for atom-photon coupling reasons we require the trap-to-toroid distance to be small. For example, using the experimental parameters of Chapter 5, we show the atom-photon coupling strength profile  $g$  in Fig. 6.11 d) showing the exponential decay profile of the toroid's evanescent field. The relevance and values at  $x_3$ ,  $x_4$ ,  $x_5$  are discussed below.

The compatibility challenge involves three key requirements that have to be satisfied simultaneously but are not necessarily compatible with each other:

- First, a good trap potential needs to be formed by the toroid-fiber composite system, taking into account: the adiabaticity requirement for the trap potential transition as the toroid-to-fiber distance decreases to the closest approach gap close to the microtoroid, moving along the fiber; the optical supermodes formed by the electromagnetic field coupling between the toroid mode and fiber mode especially at the small surface-to-surface gap distance required

(gap < 500 nm); reasonable trapping beam power ( $\approx 10$  mW), keeping in mind that the FORT beam wavelengths have to be the magic wavelengths (e.g., 687 nm, 937nm for cesium D2 line) to maintain atom transition frequency close to cavity resonance; and finally the minimum limit of toroid-to-fiber distance due to the presence of Casimir-Polder potentials that create potential ‘cliffs’ near the dielectric surfaces, destroying the optical trap potentials.

- While the first requirements argue for larger toroid-to-fiber gap distance, this second requirement necessitates smaller gap distance. In fact, here, the smaller gap may actually be better. As expected, this second requirement is required to position the trapped atom close to the toroid to achieve as strong coupling as possible. For our experimental parameters discussed in Chapter 5, with a quality factor of  $Q \sim 10^7$  leading to a total cavity decay rate of  $\kappa/2\pi = 20$  MHz, the electric field mode profile for toroid principal diameter  $D_p = 24 \mu\text{m}$  and minor diameter  $D_m = 3 \mu\text{m}$ , we have that the atom-photon coupling parameter  $g$  is equal to  $\kappa$  (i.e.,  $g/2\pi = \kappa = 20$  MHz) at atom-to-toroid distance of  $x_6-x_3 = 244$  nm. For  $g/2\pi = 30$  MHz and 45 MHz, the atom-to-toroid distances are  $(x_6-x_4) = 184$  nm and  $(x_6-x_5) = 122$  nm, respectively.
- The third, last but certainly not least requirement, is the critical coupling condition. While this requirement may not be absolutely required depending on the specific experiment, the fact is that the toroid-taper distance determines the extrinsic input-output coupling rate,  $\kappa_{\text{ex}}$ . As discussed in detail in Sec. 3.1.1.2, not only is there only a single toroid-taper distance that provides critical coupling, but this location is quite sensitive to exact fabrication parameters such as the principal diameter of toroid and nanofiber diameter, see Fig. 3.2. With the  $\approx 5$ -10% microtoroid dimensions fabrication uncertainty and  $\approx 5\%$  nanofiber diameter fabrication uncertainty, this third requirement presents a significant constraint.

As can be seen from the above, the integration of a microtoroid cavity with a single nanofiber facilitating optical input-output coupling and atomic trapping involves a compatibility challenge as discussed above. While the three abovementioned requirements are each quite important and critical, they are not necessarily compatible with each other—they may not all be satisfied or optimized simultaneously. This presents a tough challenge which requires addition of more degrees of freedom to allow the three-dimensional constraints to be tuned with a sufficient number of ‘knobs’, or significant reduction in the experimental and fabrication uncertainties such that the optimization may be done at the design and fabrication stage. At a more intrinsic and fundamental design level,

one of the reasons these challenges arise is because of the fact that the composite system consists of two parts, the microtoroid cavity, and the tapered nanofiber. A possible promising candidate that offers a one-part cavity QED system is a photonic crystal cavity that is butt-coupled to an optical fiber. Within this context, we investigate and discuss cavity QED platforms using nanophotonic waveguides and cavities, discussed in Chapter 8.

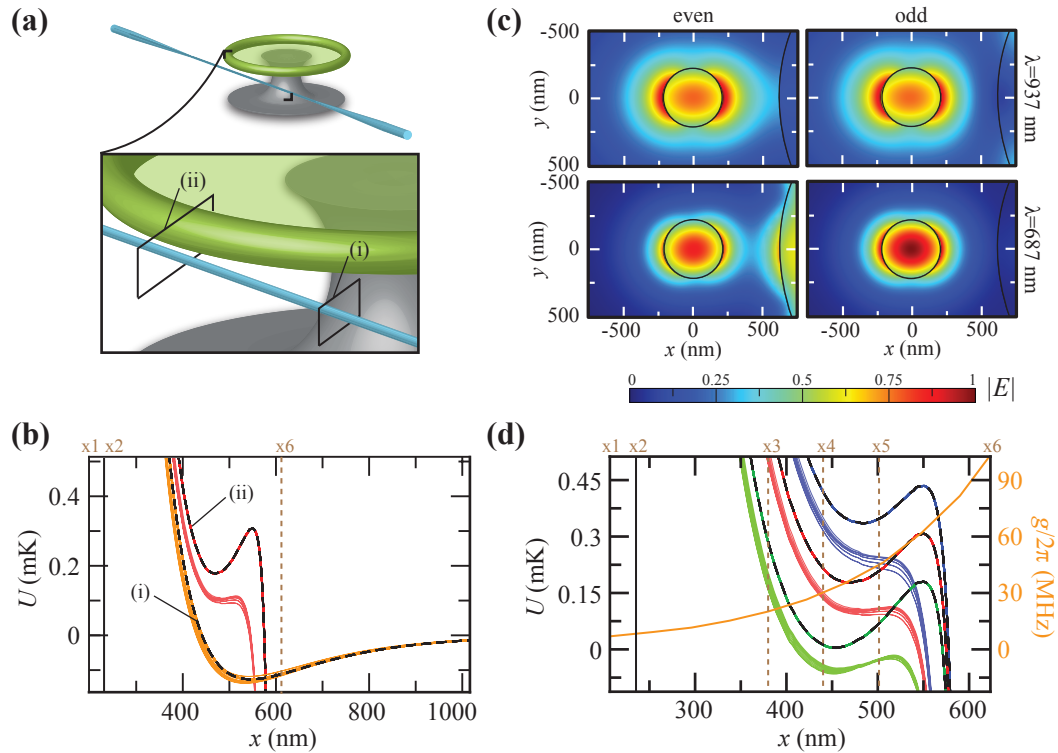


Figure 6.11: **Trapping atoms near a nanofiber and a microtoroid.** **a)** Schematic of a microtoroidal cavity and a nanofiber for trapping atoms in the evanescent field of the toroid's whispering gallery mode. **b)** Dipole trap potential  $U$  around the nanofiber far away from the toroid, using the fundamental  $HE_{11}$  mode of the nanofiber (radius  $a = 215$  nm) is shown by curve (i) in a) and b). The left end of the plot is at  $x = x_1 = 215$  nm (the fiber's surface), while  $x = x_6$  is the toroid's surface for the trap potential curve (ii) in b) and a), which takes into account the even and odd supermodes as equal superpositions. The almost vertical line at  $x = x_2$  represents the Casimir-Polder potential 'cliff' that diverges to  $-\infty$  at the nanofiber surface. **c)** Electric field amplitude  $|E|$  profiles for the lowest order even and odd supermodes for  $\lambda = 687$  nm and  $937$  nm, treating the nanofiber and toroid as two silica parallel cylindrical waveguides with diameters  $430$  nm and  $3 \mu\text{m}$  respectively. **d)** Trap potentials,  $U$ , at the closest approach plane (ii) in a), for  $F=4$  ground state (thick colored curves),  $F=3$  ground states (black dashed curves), and  $F'=4$  excited states (thin colored curves). The same set of red curves are shown in b) and d). The orange curve in d) shows the atom-toroid coupling rate  $g$ , with  $g/2\pi = 20, 30, 45$  MHz at  $x_3, x_4, x_5$  respectively. A typical experimental value for the total cavity decay rate achieved for the toroid geometry considered as described in Chapter 5 is  $\kappa/2\pi = 20$  MHz.